SANDIA REPORT
SAND2002-0524
Unlimited Release
Printed March 2002

Frozen Soil Material Testing and Constitutive Modeling

Moo Y. Lee, Arlo Fossum, Laurence S. Costin and David Bronowski

Prepared by
Sandia National Laboratories
Albuquerque, New Mexico 87185 and Livermore, California 94550

Sandia is a multiprogram laboratory operated by Sandia Corporation, a Lockheed Martin Company, for the United States Department of Energy under Contract DE-AC04-94AL85000.

Approved for public release; further dissemination unlimited.

Issued by Sandia National Laboratories, operated for the United States Department of Energy by Sandia Corporation.

NOTICE: This report was prepared as an account of work sponsored by an agency of the United States Government. Neither the United States Government, nor any agency thereof, nor any of their employees, nor any of their contractors, subcontractors, or their employees, make any warranty, express or implied, or assume any legal liability or responsibility for the accuracy, completeness, or usefulness of any information, apparatus, product, or process disclosed, or represent that its use would not infringe privately owned rights. Reference herein to any specific commercial product, process, or service by trade name, trademark, manufacturer, or otherwise, does not necessarily constitute or imply its endorsement, recommendation, or favoring by the United States Government, any agency thereof, or any of their contractors or subcontractors. The views and opinions expressed herein do not necessarily state or reflect those of the United States Government, any agency thereof, or any of their contractors.

Printed in the United States of America. This report has been reproduced directly from the best available copy.

Available to DOE and DOE contractors from
U.S. Department of Energy
Office of Scientific and Technical Information
P.O. Box 62
Oak Ridge, TN 37831

Telephone: (865)576-8401
Facsimile: (865)576-5728
E-Mail: reports@adonis.osti.gov
Online ordering: http://www.doe.gov/bridge

Available to the public from
U.S. Department of Commerce
National Technical Information Service
5285 Port Royal Rd
Springfield, VA 22161

Telephone: (800)553-6847
Facsimile: (703)605-6900
E-Mail: orders@ntis.fedworld.gov
Online order: http://www.ntis.gov/ordering.htm

SAND 2002-0524
Unlimited Release
Printed March 2002

Frozen Soil Material Testing and Constitutive Modeling

Moo Y. Lee, Arlo Fossum, Laurence S. Costin, and David Bronowski
Geomechanics Department

Joseph Jung
Thermal Environments Department

Sandia National Laboratories
P.O. Box 5800
Albuquerque, NM 87185-0751

ABSTRACT

To obtain a well-determined constitutive database for the Alaskan frozen soil at confining pressures up to 100 MPa and temperatures down to –25°C, a series of laboratory tests was conducted using a unique high-pressure, low-temperature apparatus and the split Hopkinson pressure bar (SHPB). Quasi-static compression tests and indirect tension (or Brazilian) tests, are required to constrain the variabilities of material properties of frozen soil. The SHPB tests are required to obtain dynamic compression properties and the strain rate dependency of the frozen soil. The results from laboratory material testing showed that Alaskan frozen soil exhibits pressure and temperature dependence, rate sensitivity, anisotropy, brittle and ductile behavior, volumetric compaction, and dilation. The rate-sensitive and anisotropic version of a plasticity model, being developed by Fossum and Fredrich (2000), was able to represent the deformation behavior of such a complex material very well. This model includes high strain-rate sensitivity and anisotropy in both the elastic and plastic regimes. The model is defined through a continuous yield and loading surface for unified dilation and compaction phenomena. It is envisioned that this model will be used to predict the deformation and failure of frozen soil under the dynamic loading conditions resulting from projectile penetration into frozen soil targets.

ACKNOWLEDGEMENTS

The authors would like to acknowledge Ned Hansen of Sandia National Laboratories for arranging the sampling activities in the Yukon Test Range at Eielson Air Force Base in Alaska. The authors also appreciate the laboratory assistance of Robert Hardy and Mark Grazier of Sandia National Laboratories. The managerial support received from Jaime L. Moya and Justine E. Johannes are also gratefully appreciated.

Table of Contents

Figures

Tables

1. Introduction

The current computational model for projectile penetration into frozen soil includes a realistic and general rock and soil materials model (Fossum and Fredrich, 2000). This model is an anisotropic, continuous, three-invariant, single-surface dilation/compaction plasticity model with mixed hardening and limit-state weakening. It is envisioned that this model will be used to predict the deformation and failure of frozen soil under the static and dynamic loading conditions resulting from projectile penetration. To predict the behavior of the frozen soil based on the model calculation, the necessary material constants must be estimated from a database populated from laboratory tests, conducted at the requisite conditions on frozen soil specimens.

However, there is little understanding of the mechanics of penetration of frozen soil that are inhomogeneous, highly variable on almost any scale and have large uncertainties associated with basic material properties. Moreover, only sparse data are available from triaxial compression experiments (Gratz and Schulson, 1996; Chamberlain et. al, 1972) conducted at the Cold Regions Research and Engineering Laboratory (CRREL) and Dartmouth College, on artificial frozen soil samples and on frozen soil obtained from the Yukon Range at Fort Wainwright, Alaska.

The objective of this project was to establish a well-determined set of constitutive data from quasi-static, quasi-dynamic, and dynamic tests on Alaskan frozen soil. These tests were to be conducted using the unique high-pressure, low-temperature apparatus (Zeuch et. al, 1999) and the split Hopkinson pressure bar (SHPB).

To estimate the material properties for implementation and validation, several types of quasi-static and dynamic SHPB tests were required. Quasi-static compression tests and indirect tension (or Brazilian) tests, were required to constrain the variabilities of material properties of frozen soil. The SHPB tests were required to obtain dynamic compression properties and the strain rate dependency of the frozen soil. The experimental program for the Alaskan frozen soil is composed of:

- A suite of quasi-static hydrostatic compression tests to determine the elastic bulk modulus, K, and the isotropic hardening parameters.
- A set of quasi-static triaxial compression tests to determine the shear modulus, shear failure properties, and yield surface shape.
- A series of Brazilian tests to determine the appropriate tension cut-off.
- A series of SHPB experiments. Deformation of the Alaskan frozen soil at strain rates up to 10^3 /s was evaluated at different temperatures. It was postulated that because of the nature of the deformation mechanisms in frozen soils, there would be a direct relationship between the effect of temperature and strain rate on the behavior of the soil. If the trade-off relationship between the temperature and strain rate is established, the behavior of frozen soil under dynamic loading conditions should be well understood by quasi-static tests conducted at a lower temperature.
- A series of quasi-dynamic loading tests that will bridge the gap in loading rates used for the quasi-static triaxial test at 10^{-5} /s and the SHPB experiments up to 10^3 /s.

Table 1. Planned test matrix for the laboratory constitutive testing of Alaskan frozen soil.

Test Type	Temperature (° C)	No. of Tests Planned	Loading Path	Test Control
Hydrostatic compression	-25° C	5	A	Pressure control 0.03 MPa/s
Uniaxial compression	-25° C -10° C	5	B	Strain control 10^{-4} to 10^{-1}
Deviatoric compression	-25° C	20	C, D	Strain control 10^{-4}
Indirect tension (Brazilian)	-25° C -10° C	20	E	Stroke control 10^{-3} mm/s
Split Hopkinson bar testing	-25° C -10° C	20	B	Up to 10^{3} /s strain rate
Quasi-dynamic compression	-25° C -10° C	10	B	Up to 10 /s strain rate

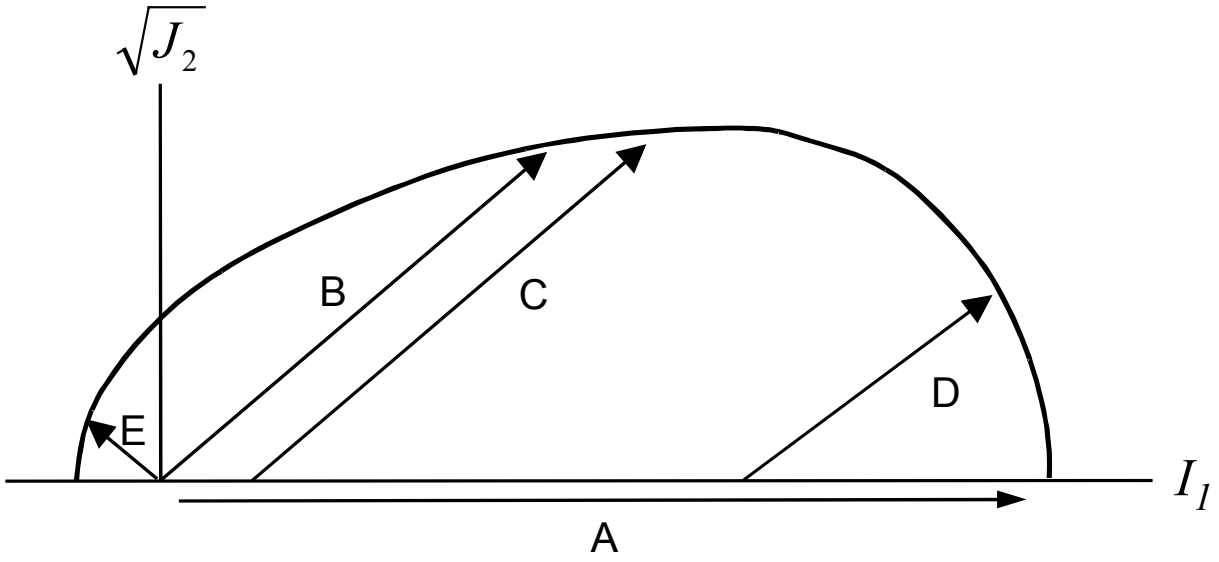

Figure 1. Summary of loading paths used for laboratory testing of frozen soil for constitutive modeling. I_1 is the first invariant of the Cauchy stress tensor and J_2 is the second invariant of the deviatoric stress tensor. Two invariants are defined as $I_1 = \sigma_1+\sigma_2+\sigma_3$ and $J_2=\{(\sigma_1 - \sigma_2)^2 + (\sigma_2 - \sigma_3)^2 + (\sigma_3 - \sigma_1)^2\} / 6$ where σ_1, σ_2 and σ_3 are the maximum, intermediate and minimum principal compressive stresses, respectively.

The experimental matrix shown in Table 1 and Figure 1 was used to construct the constitutive database for the frozen soil at confining pressures up to 100 MPa and temperatures down to –25°C. Once a data set with sufficient information is constructed, an assessment can be made of the adequacy of the material model to represent the deformation of frozen soil under penetrating projectile conditions. The data, along with a suitable numerical constitutive model, are critical in predicting the behavior of penetrator weapons into frozen soil targets.

2. Sample Preparation and Characterization

2.1 Sample preparation

The frozen soil cores were extracted from FTU-11-18 and FTU-11-24 sites in the Yukon Test Range at Eielson Air Force Base in Alaska. The US Army Cold Regions Research and Engineering Laboratory conducted sampling activities using a 7.6 cm diameter coring auger kit developed by CREEL (Ueda et. al, 1975). The coring auger was specially designed for sampling undisturbed fine-grained frozen soils near the earth's surface in the cold regions. The extracted cores were shipped in a cooler to Sandia National Laboratories and stored in a freezer at –10° C. The diameter of the core was 7.6 cm and the length of the core measured from the surface was approximately 80 cm.

A water-jet cutting technique was used to extract smaller diameter core specimens from the 7.6 cm core. Initially, a drill bit, cooled by liquid nitrogen, was used. However, the drill bit showed a tendency to get jammed when used in fine-grained frozen soils because of lost circulation of coolant and accumulation of soil cuttings around the bit. Consequently, it was impossible to extract undisturbed small diameter core specimens. The water-jet cuts the specimen using the stream of high pressure (approximately 400 MPa) water, mixed with abrasives exiting the small diameter nozzle. We used the nozzle with 0.03 cm orifice in diameter. The narrow stream of the water-jet creates fewer disturbances to the specimens than drilling with a core barrel.

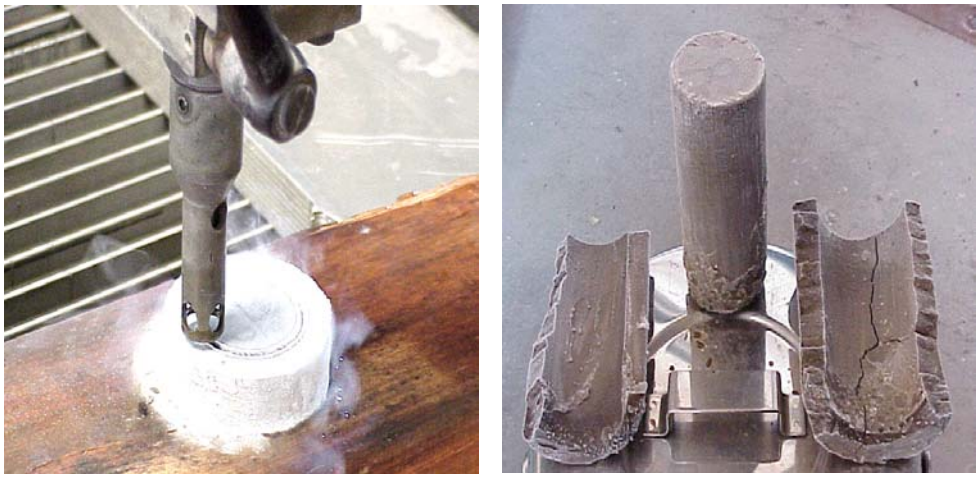

Figure 2. Water-jet cutting of cylindrical specimen from the frozen soil core.

Figure 2 shows water jet coring used for preparing a cylindrical specimen from frozen soil cores. The extracted specimen was then cut perpendicular to the longitudinal axis of the core, using a diamond saw cooled by liquid nitrogen.

A spring-loaded V-block (Figure 3) design, based on the principle of pressure melting, was used to ensure the ends of the cylindrical specimens were prepared perpendicular to the axis of the specimen and parallel to each other. The specimen was mounted between the cylindrical end-caps and the assembly was placed on the V-block. The spring-loaded clamp applies the axial force to the specimen. The pressure melting occurs between the ends of the specimen and the end-caps. This allows the frozen soil specimen to be mounted with its ends parallel to each other and perpendicular to the axis of the specimen.

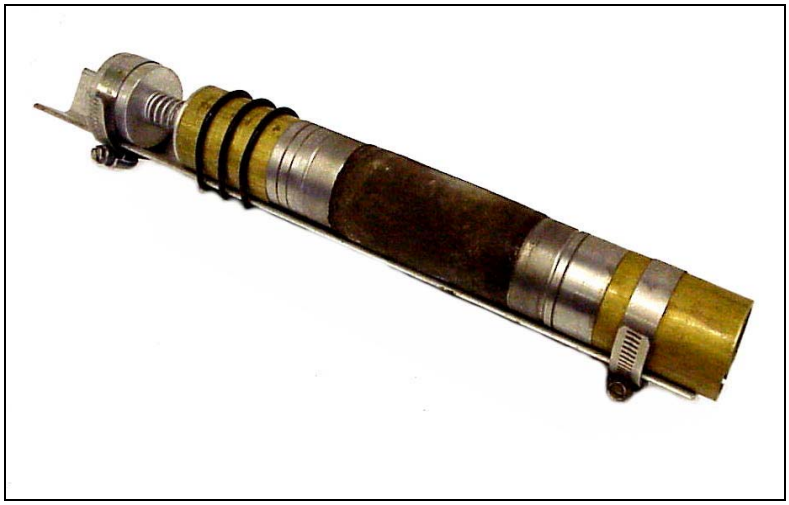

Figure 3. Spring-loaded V-block apparatus used to mount the end-caps to the frozen soil specimen.

Brazilian test specimens were prepared to have nominal dimensions of 75 mm in diameter and 38 mm in thickness. The dimensions fall in the range (0.2 to 0.75) of thickness-to-diameter ratio recommended in ASTM D3967 ("Standard Test Method for Splitting Tensile Strength of Intact Rock Core Specimens").

We fabricated right cylindrical specimens of frozen soil for hydrostatic, uniaxial and triaxial compression tests following ASTM D4543 ("Standard Practice for Preparing Rock Core Specimens and Determining Dimensional and Shape Tolerances"). The specimens have the nominal dimension of 45 to 55 mm in diameter and 90 to 115 mm in length. The dimensions fall within the range of length-to-diameter ratio (2 to 2.5) recommended in ASTM D4543 for testing other types of materials.

Small diameter (approximately 22 mm) disk specimens were also prepared for the SHPB and quasi-dynamic testing. The same procedures were used as those used to prepare the Brazilian test specimens. The SHPB specimens were prepared to match the diameter of the incident and transmission bars used in SHPB testing.

2.2 Sample characterization

Extracted core specimens from the Alaskan frozen soil showed distinct contrast (see Figure 4) in basic physical characteristics, such as color, density and water content. Table 2 and Figure 4 summarize the variations of water content in the Alaskan frozen soil with respect to depth. Specimens extracted near the surface (sample ID's ending with A) showed approximately 85 weight % water content. In contrast, the specimens extracted at depth away from the surface (sample ID's ending other than A) showed 42 weight % of water content on average.

The solid constituents of the near-surface frozen soil were mostly organic materials such as plant roots, wood debris, etc., represented by dark colors. The constituents of the frozen soil from below 30 cm in depth were mainly clay and silt particles represented by the light colors (Figure 4).

Variations of water content and solid constituents with respect to depth resulted in the variations of densities of the Alaskan frozen soil (Figure 5). The low density (<1 g/cm^3) frozen soil with abundant organic materials was usually found within 30 cm from the surface. The high density (>1 g/cm^3) frozen soil was found from the depth greater than 30 cm.

Table 2. Variations of water content with respect to depth in the Alaskan frozen soil.

Sample I.D	Test I.D	Depth (m)	Total Weight (g)	Solid weight (g)	Solid content (weight %)	Water content (weight %)
AFS-12-C	AFS-TA-14	0.7	230.1	138.5	60.2	39.8
AFS-12-A	AFS-UC-05	0.2	121.4	17.7	14.6	85.4
AFS-15-G	AFS-TA-15	0.7	238.7	153.2	64.2	35.8
AFS-14-A	AFS-TA-16	0.2	141.6	21.6	15.3	84.7
AFS-14-D	AFS-HS-15	0.5	200.0	106.4	53.2	46.8
AFS-14-C	AFS-TA-13	0.4	194.4	87.5	45.0	55.0
AFS-14-G	AFS-HS-17	0.8	193.9	108.7	56.1	43.9
AFS-12-E	AFS-HS-16	0.7	225.5	137.3	60.9	39.1
AFS-15-B	AFS-TA-10	0.2	248.3	164.0	66.0	34.0

Figure 4. Alaskan frozen soil specimens extracted from different depths. The specimen on the left represents typical frozen soil found near the surface (within 30 cm in depth) with abundant organic materials. The specimen on the right shows relatively uniform clay/silt rich frozen soil found below 30 cm in depth.

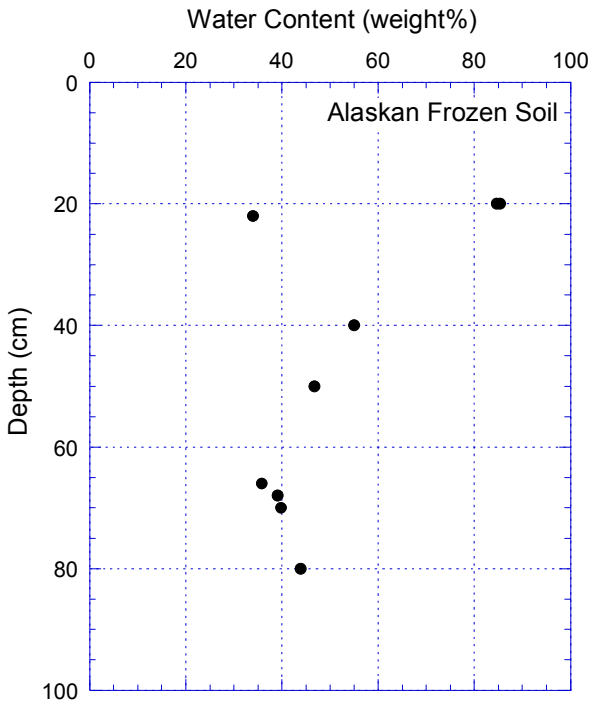

Figure 5. Water content of Alaskan frozen soil specimens extracted from different depths.

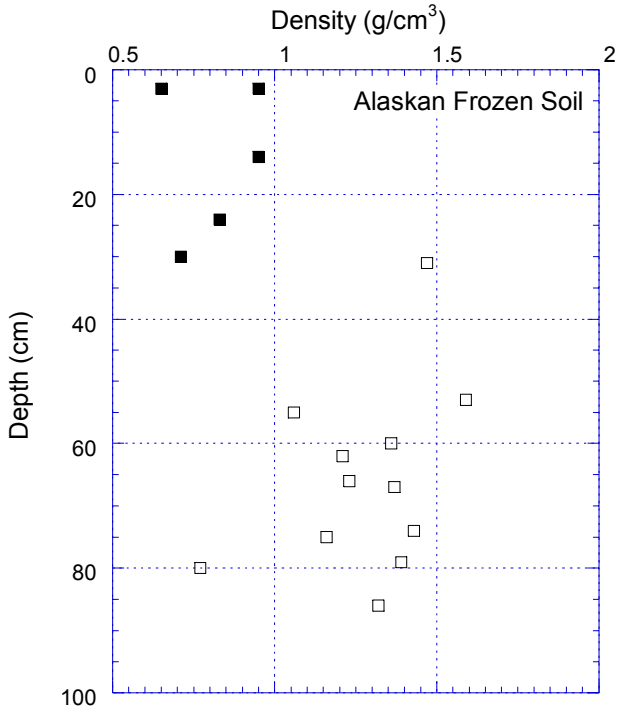

Figure 6. Densities of Alaskan frozen soil with respect to depth. The top 30 cm of the soil is dark-colored with abundant organic material.

3. Development of High-Pressure Low-Temperature (HPLT) Triaxial Test Cell

A High-Pressure Low-Temperature (HPLT) triaxial test cell was designed and built to characterize the Alaskan frozen soils at both high pressures and low temperatures. It is capable of operating at temperatures as low as –65 °C and confining pressures up to 500 MPa. The HPLT triaxial cell is able to accept cylindrical test specimens having diameters and lengths up to 4.4 and 13.2 cm, respectively. Figure 7 shows the schematic of the load frame and instrumented frozen soil specimen integrated with the HPLT test cell. In addition to the fundamental operating conditions of temperature, pressure and large specimen size required for the test cell, additional requirements and restrictions imposed serious constraints upon the design. These additional requirements included, for example, the necessity to: (1) fit in an existing, 1.9 MN servo-controlled load frame; (2) operate within an otherwise normal laboratory setting (*i.e.,* not in a cold room); and (3) use a liquid confining medium for safety and system controllability. Owing to the extreme operating conditions and the likelihood of high piston-seal friction, we also decided that internal load and strain measurements, and hence, numerous high-pressure feed-throughs, would be necessary. Nevertheless, despite these and other restrictions, it was deemed feasible to use an externally cooled pressure vessel (Figure 8), composed of HP9-4-20 alloy steel and equipped with twelve coaxial feed-throughs. Two specially designed load cells have been built for internal force measurements. Strains were measured using the LVDTs mounted in special fixtures.

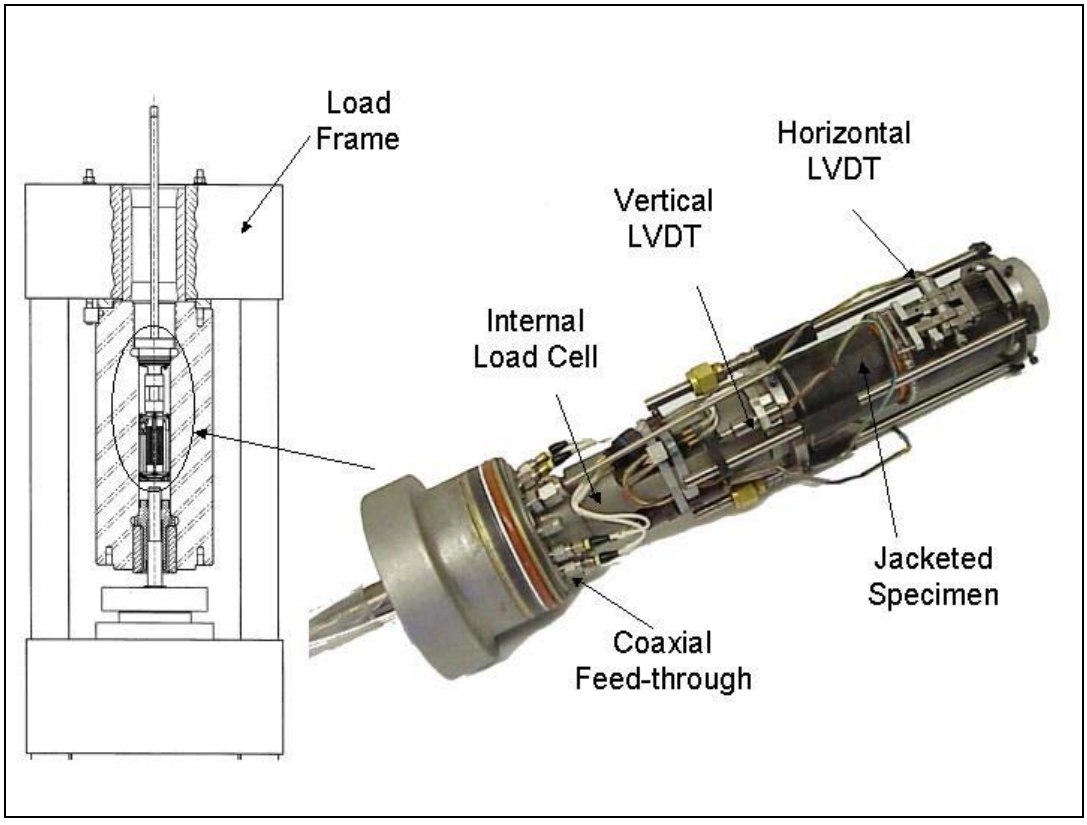

Figure 7. Schematic of the High-Pressure Low-Temperature test cell and an instrumented frozen soil specimen.

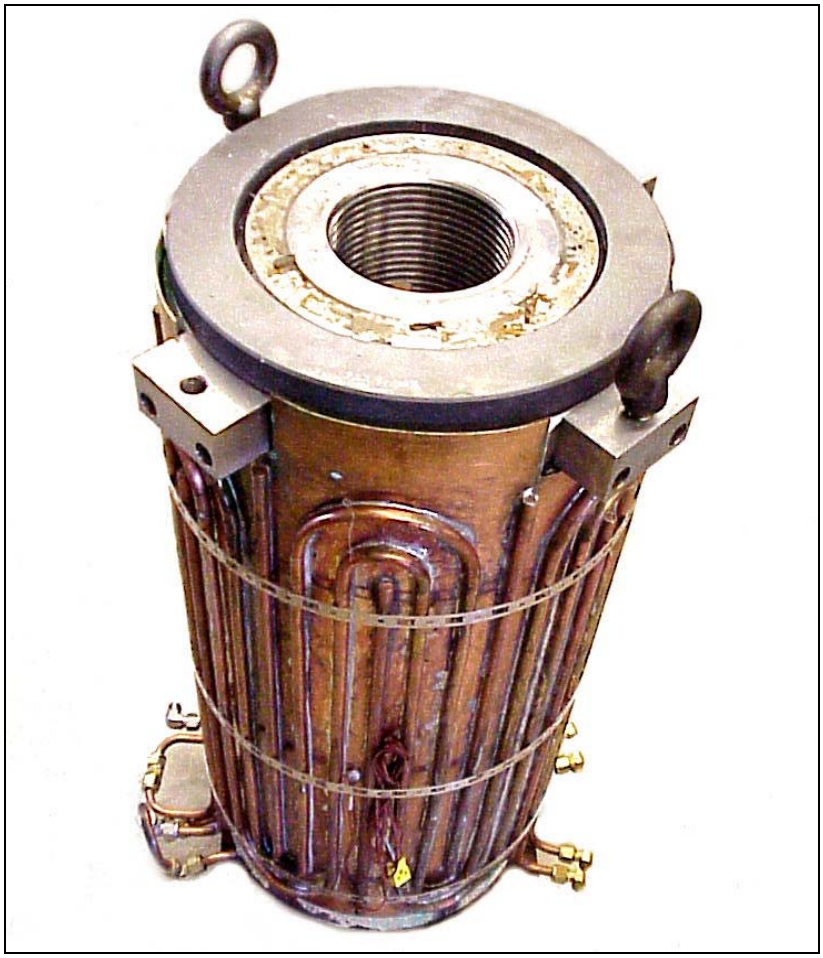

Figure 8. External cooling system implemented for the High-Pressure Low-Temperature (HPLT) cell.

4. Constitutive Testing

4.1 Hydrostatic compression tests

A cylindrical specimen, prepared following the ASTM D4543, was used to measure the bulk modulus, K, of the frozen soil. A typical frozen soil specimen prepared for hydrostatic compression test is shown in Figure 9. After the specimen was jacketed in a neoprene jacket and instrumented with LVDT's, the assembly was inserted in the HPLT test cell (Figure 7). The push rod, used for applying the axial load to the specimen, was pulled back so as not to apply any deviatoric stress to the specimen. The confining pressure, P, was increased all around the specimen to apply all three principal stresses $\sigma_1=\sigma_2=\sigma_3=P$ hydrostatically to the specimen. The pressure was measured with the pressure transducer connected to the HPLT test cell and the axial and lateral displacements were measured with the vertical and horizontal LVDT's, respectively (Figure 7). The loading history of the hydrostatic compression is represented by the loading path A in I_1 vs. $J_2^{0.5}$ plot shown in Figure 1.

Figure 9. Frozen soil specimen mounted between the end-caps for hydrostatic compression test.

The strains (axial, lateral, and volumetric) vs. pressure plot, recorded during compression of AFS-HS-12 Alaskan frozen soil specimen, is shown in Figure 10. A detailed unloading and reloading loop conducted around the 50 MPa pressure level in test AFS-HS-12 is also shown in Figure 11. A linear regression analysis was conducted to the data corresponding to unloading and reloading a portion of the curve. The slope of the best-fit straight line determines the bulk modulus, K, defined as the ratio between the hydrostatic pressure P and the volumetric strain $\Delta V/V$ it produces (Jaeger and Cook, 1969).

$$K = P / (\Delta V/V)$$

where the volumetric strain, ΔV, is calculated as the sum of axial strain, ε_a and two times the lateral strain, ε_l. The reciprocal of the bulk modulus is called the compressibility $\beta=1/K$.

It was noticed that the axial strain from AFS-HS-12 test deviates from the linear trend around 100 MPa of confining pressure. As suggested from the phase diagram of ice (Durham et. al, 1983) shown in Figure 12, the deviation of the axial strain may indicate the phase change or pressure melting of the ice imbedded, as the lenticular structure of the soil. The change of phase in ice under high confining pressure may play an important role in modeling the frozen soil target coupled with the projectile penetration into it. Depending on the accumulated pressure surrounding the penetrator and the temperature changes in the target, the frozen soil should be modeled considering the phase changes of the imbedded ice.

It was also noticed that the frozen soil in test AFS-HS-07 (Figure 13) deformed in an anisotropic manner. The axial strain was approximately two times larger than that of the lateral strain. The anisotropic deformation in frozen soil was expected since it contains wind-blown clay/silt particles, sometimes forming a bedding structure. Ice provides a mechanical bond between soil particles and sometimes between bedding planes.

Table 3 summarizes the results from the hydrostatic compression tests. The bulk modulus of the frozen soil ranges from 9 to 35 GPa. The average bulk modulus was 21.8 (±7.7) GPa. The variations of the bulk modulus, with respect to depth, temperature and density of the Alaskan frozen soil, are shown in Figure 14. Because of the inhomogeneity of the frozen soil, the bulk modulus had wide variations, up to 25 GPa, for the identical test condition. In Figure 14, we can also see that under the same temperature condition (-10°C), the bulk modulus of the frozen soil appears to increase with the density of the soil. Other factors, such as depth and temperature, evidently were not associated with the bulk modulus.

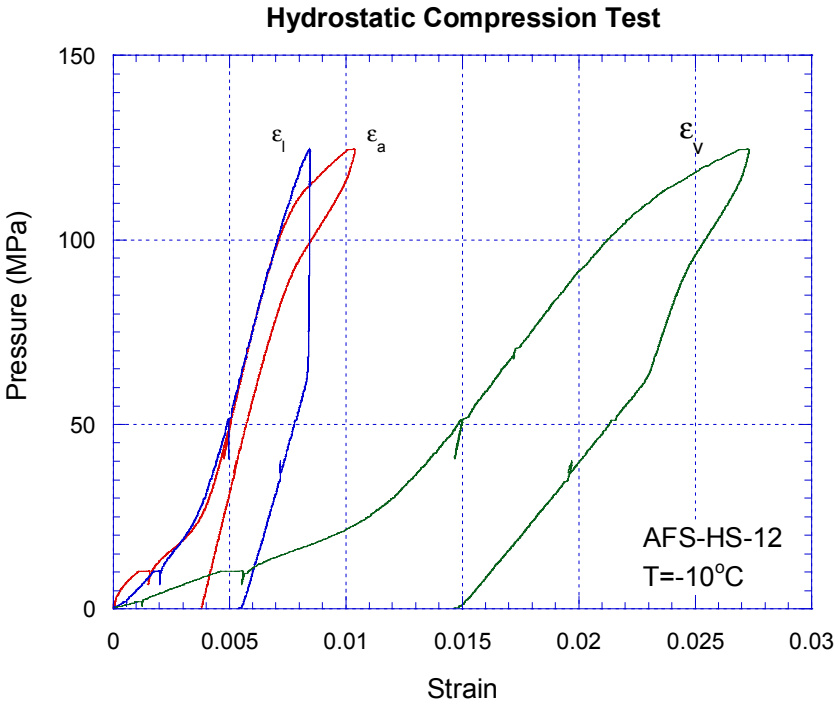

Figure 10. Strain vs. hydrostatic pressure recorded during a hydrostatic compression testing of a frozen soil specimen.

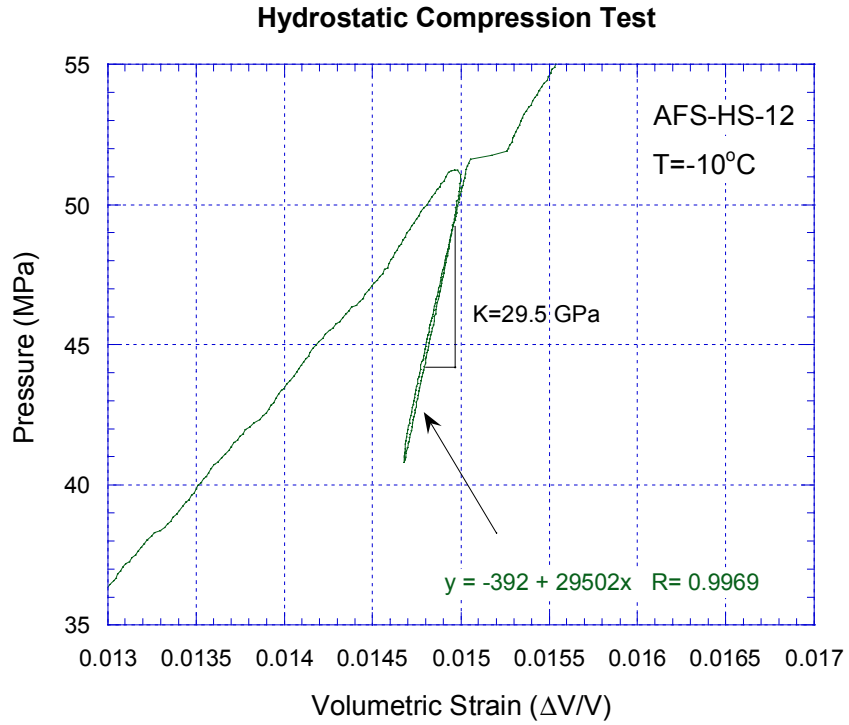

Figure 11. Detailed volumetric strain vs. hydrostatic pressure plot showing unloading and reloading loops for the frozen soil specimen AFS-HS-12. The slope of the loop determines the bulk modulus, K.

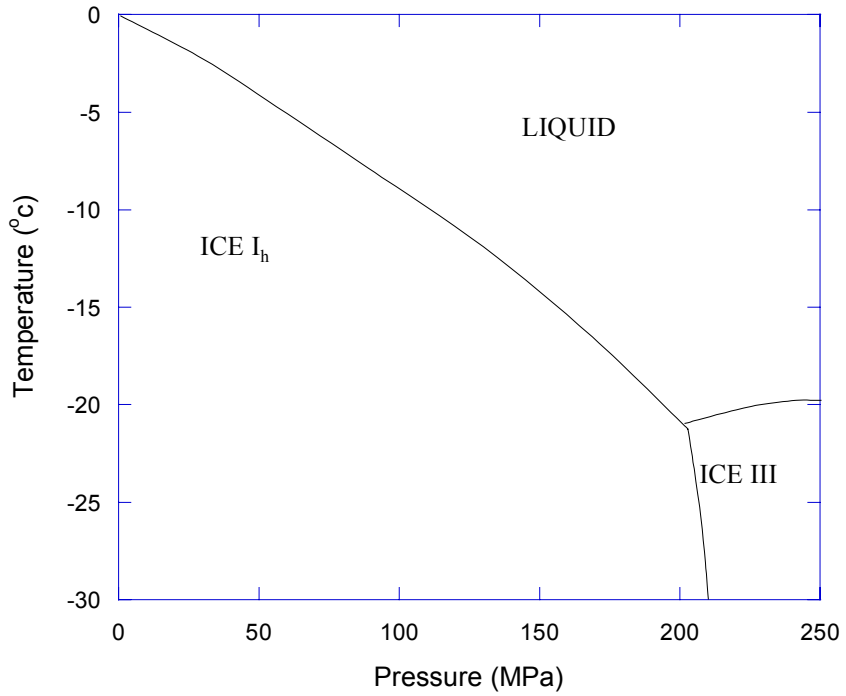

Figure 12. Phase diagram for ice under different pressures and temperatures based on Durham et. al. (1983).

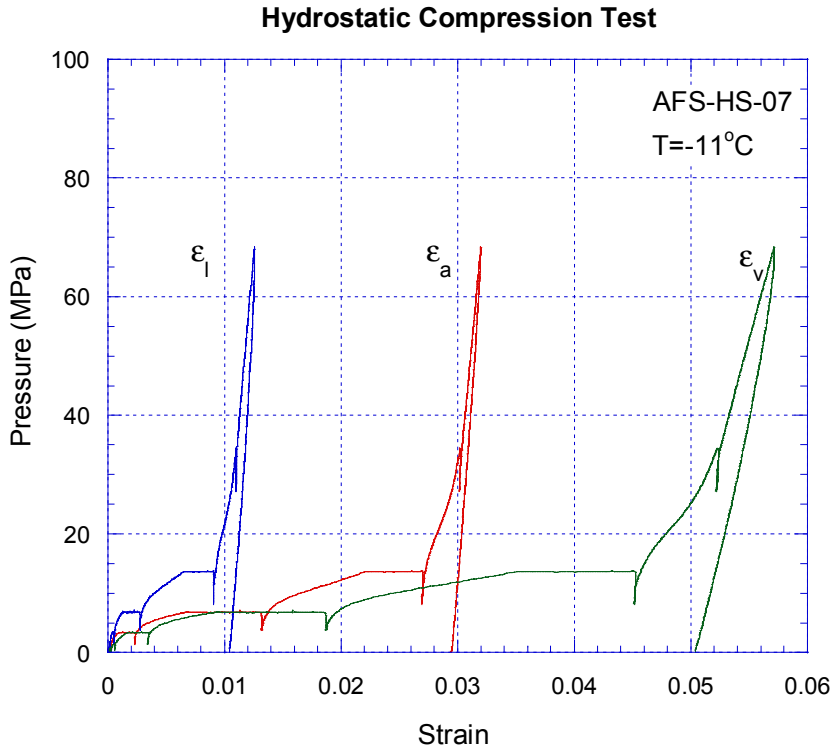

Figure 13. Strain vs. hydrostatic pressure recorded during a hydrostatic compression testing of an anisotropic frozen soil specimen.

Table 3. Summary of hydrostatic compression tests of Alaskan frozen soil.

Test No.	Sample Location	Depth (m)	Diameter (mm)	Length (mm)	Weight (g)	Density (g/cm^3)	Temperature (C)	P_{max} (MPa)	P_{bm} (MPa)	K (GPa)
AFS-HS-01	AFS-08-D	0.3	44.5	101.3	250	1.59	-23.9	29.0	NA	NA
AFS-HS-02	AFS-03-B	0.2	44.5	99.1	NA	NA	-9.4	30.0	21	20.2
AFS-HS-03	NA	NA	NA	NA	NA	NA	-10.2	14.5	NA	NA
AFS-HS-04	AFS-02-F	0.7	43.9	92.2	NA	NA	-10.2	68.7	30	34.9
AFS-HS-05	AFS-02-E	0.5	43.9	92.2	NA	NA	-10.4	13.7	NA	NA
AFS-HS-06	AFS-01-D	0.4	44.2	99.1	NA	NA	-10.5	20.5	20*	21.0
AFS-HS-07	AFS-05-E	0.5	44.5	97.0	NA	NA	-10.9	68.4	33	23.7
AFS-HS-08	AFS-09-D	0.7	44.5	101.3	225	1.43	-10.9	68.3	33	24.8
AFS-HS-09	AFS-09-E	0.8	44.2	101.6	199	1.28	-12.0	68.0	NA	NA
AFS-HS-10	AFS-10-B	0.2	44.2	100.3	198	1.29	-10.5	68.8	51	18.3
AFS-HS-11	AFS-11-F	0.8	44.5	101.9	239	1.51	-10.5	68.3	51	33.8
AFS-HS-12	AFS-10-C	0.3	44.5	100.3	238	1.53	-10.4	124.9	51	29.5
AFS-HS-13	AFS-15-E	0.5	44.2	103.6	NA	NA	-10.5	142.1	95	21.0
AFS-HS-14	AFS-12-F	0.8	44.2	101.1	223	1.44	-6.2	68.2	68*	17.1
AFS-HS-15	AFS-14-D	0.5	43.9	102.9	203	1.30	-25.1	138.2	138*	19.2
AFS-HS-16	AFS-12-E	0.7	44.2	100.3	227	1.47	-6.0	68.2	68	10.3
AFS-HS-17	AFS-14-G	0.8	44.5	99.3	202	1.31	-25.6	68.2	68	9.2

P_{max} -maximum hydrostatic pressure applied.

P_{bm}-level of hydrostatic pressure at which Bulk Modulus, K, is obtained.

K-bulk modulus

*- bulk modulus was obtained at the maximum hydrostatic pressure applied to the specimen.

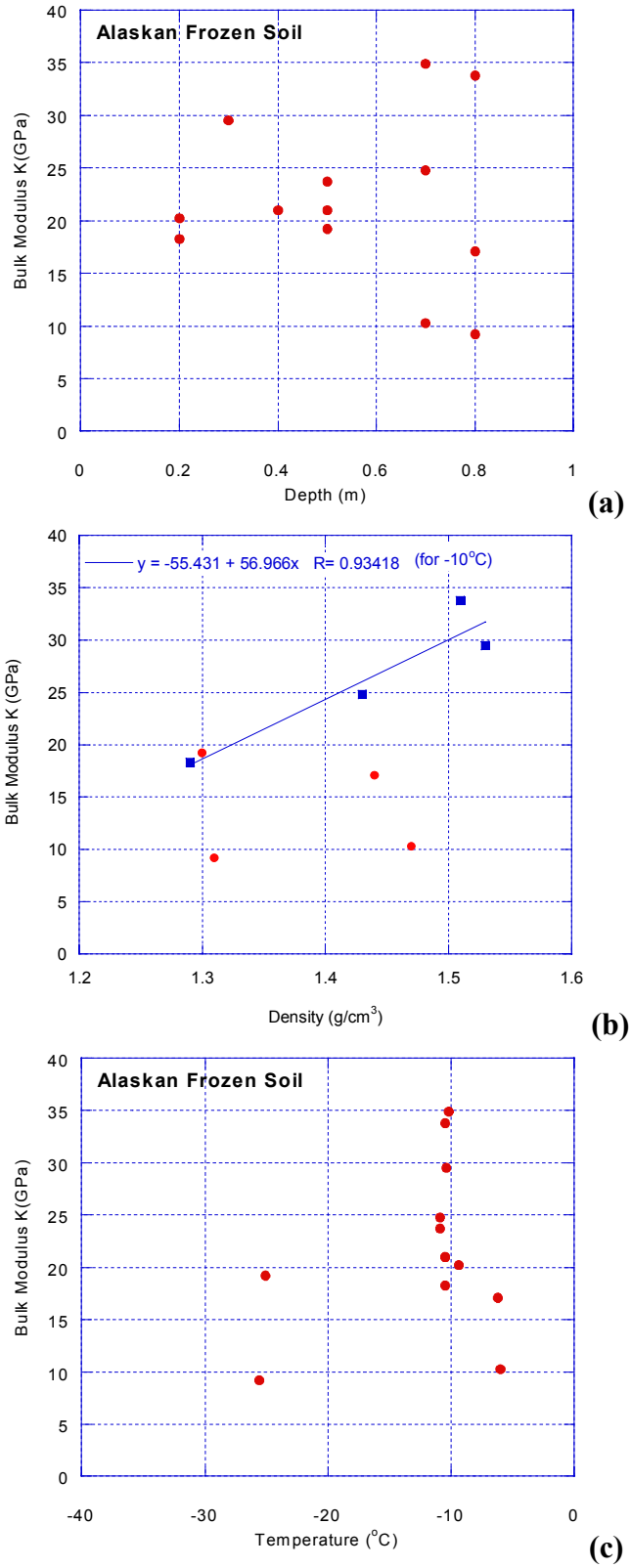

Figure 14. Variations of the bulk modulus of Alaskan frozen soil with respect to **(a)** depth **(b)** density and **(c)** temperature.

4.2 Brazilian tests

To measure indirect tensile strengths of the Alaskan frozen soil, the prepared specimens were diametrically loaded in the environmental chamber, shown in Figure 15. The indirect Brazilian test followed the loading path E in I_1 vs. $J_2^{0.5}$ plot, shown in Figure 1. The temperature in the chamber is controlled by forced circulation of liquid nitrogen. The thermocouple, inside the chamber, constantly measures the air temperature in the chamber and provides feedback signal to the temperature controller. Two through-wall ports, opened in the vertical direction of the chamber, accommodate loading rods.

The loading axis of the specimen was marked by a diametral line on each end of the specimen. The specimen was centered in the loading machine using the diametral marking. The compressive line load was applied to the specimen at an approximately constant displacement rate of 0.05 mm/s. The tensile failure of the specimens occurred at approximately one minute of loading. The displacement control allows us to capture the complete load-displacement record to peak load without overloading the specimen.

Three channels of time, load and axial displacement were recorded using a DATAVG data acquisition program (Hardy, 1993). Figure 12 shows the 0.1 MN servo-controlled loading system set-up for Brazilian test.

The indirect tensile strength of the frozen soil was calculated from:

$$T_{br} = 2P_{br}/\pi tD$$

where T_{br} is the indirect tensile strength in MPa; P_{br} is the peak load in N; t is the thickness of the circular core in mm and D is the diameter of the specimen in mm.

Figure 15. Brazilian indirect tensile strength test set-up. Shown are the 0.1 MN servo-controlled loading machine, data acquisition system and a failed specimen.

Diametral line loading of the specimens created two different types of fractures as shown in Figure 16. A typical extension fracture (Figure 16a) along the loading axis of the specimen was observed under the conditions of low temperature (-26°C) and low displacement rate (0.05 mm/s). Brittle tensile fracture is the result of the tensile stress, T_{br} , acting perpendicular to the fracture plane. Initiation of the fracture is represented as a peak load, followed by an abrupt drop of the load in the displacement vs. load plot (Figure 17).

When the temperature was increased to approximately –10°C, the specimen underwent a large amount of plastic deformation before the extension fracture developed. In this relatively higher temperature condition, the specimen did not fail in tensile stress generated by the diametral line load. As the contact area between the specimen and the loading platen increases, the basic assumption of line loading to create uniform T_{br} becomes invalid. The characteristics of the Brazilian test resembled those of the uniaxial compression tests. As shown in Figure 16b, a network of shear fractures was formed under the condition of high temperature. Typical displacement vs. load record at -10°C is shown in Figure 18. The load increased monotonically without a peak load.

In AFS BR-12 test, the displacement rate was increased on order of magnitude to 0.5 mm/s while the temperature was maintained at -10°C. The higher displacement rate (0.5 mm/s) resulted in brittle tensile fracture at -10°C. This experiment suggests that a trade-off exists between the temperature and the displacement rate in the Brazilian tensile strength. Table 4 summarizes the results from Brazilian tensile tests conducted on the Alaskan frozen soil under two levels of temperature. Based on the Brazilian tensile tests, it was concluded that the brittle-ductile transition may have been influenced by the temperature and displacement rate.

(a) (b)

Figure 16. Two different types of fracturing behavior of the Alaskan frozen soil subjected to diametral loading. AFS-BR-17 specimen (a) shows brittle tensile fractures under the low temperature condition (-26°C). AFS-BR-11 specimen (b) shows the network of ductile fractures, with a large amount of plastic deformation under the high temperature condition (-9°C).

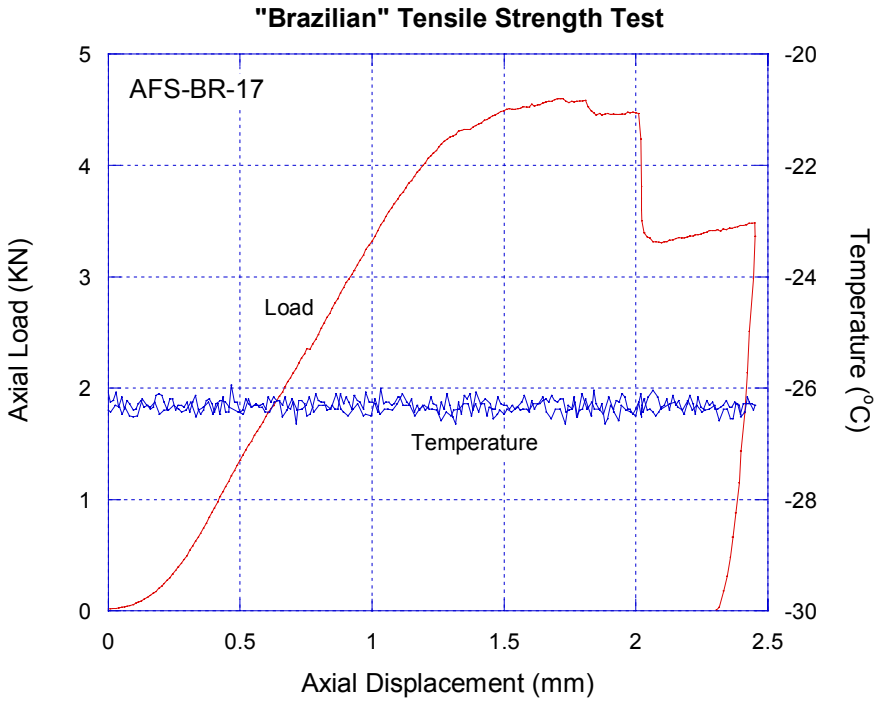

Figure 17. Typical displacement vs. load record from a Brazilian test conducted for the Alaskan frozen soil at approximately –26°C.

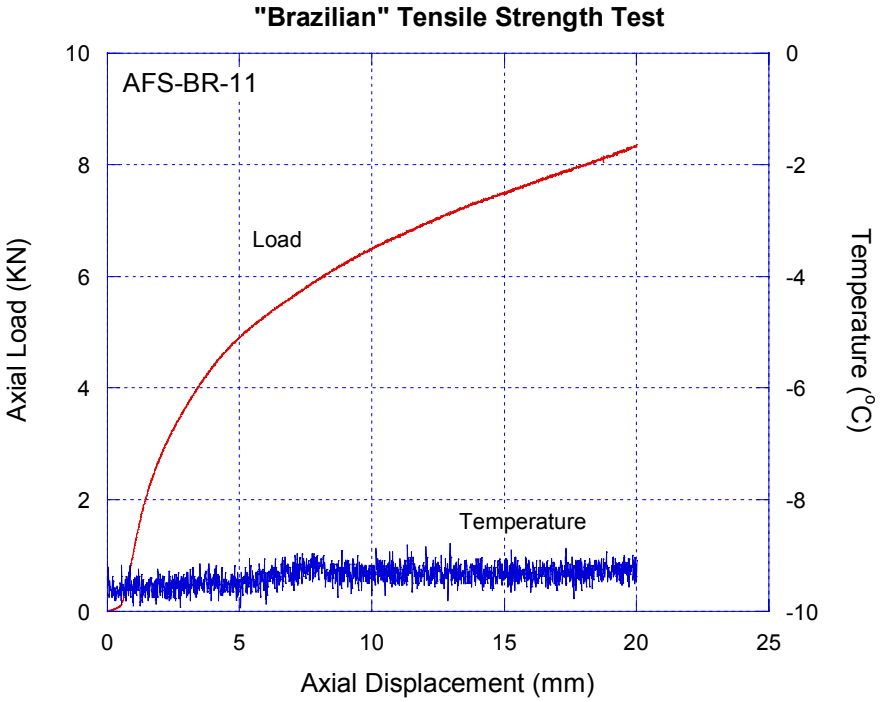

Figure 18. Typical displacement vs. load record from a Brazilian test conducted for the Alaskan frozen soil at approximately –10°C. Load increased monotonically without a peak, indicating a ductile deformation without a brittle tensile failure.

Table 4. Summary of Brazilian tensile tests of Alaskan frozen soil under two different temperature conditions.

Test No.	Sample Location	Depth (m)	P_{br} (kN)	Diameter (mm)	Thickness (mm)	Weight (g)	Density (g/cm^3)	Temperature (ºC)	Displacement Rate (mm/s)	T_{br} (MPa)
AFS-BR-01	AFS-05-A	0.8	NA	74.8	27.5	93	0.77	-11.0	0.01	NA
AFS-BR-02	AFS-01-F	0.6	NA	74.6	43.4	258	1.36	-11.1	0.05	NA
AFS-BR-03	AFS-05-F	0.6	NA	75.1	39.1	210	1.21	-9.0	0.05	NA
AFS-BR-04	AFS-02-C	0.2	NA	74.3	37.3	134	0.83	NA	0.05	NA
AFS-BR-05	AFS-01-H	0.8	NA	75.3	38.9	240	1.39	-9.9	0.05	NA
AFS-BR-06	AFS-03-C	0.3	NA	74.8	42.7	275	1.47	-12.4	0.05	NA
AFS-BR-07	AFS-03-F	0.7	NA	75.1	42.0	228	1.23	-11.3	0.05	NA
AFS-BR-08	AFS-05-G	0.8	NA	75.2	32.5	168	1.16	-11.2	0.05	NA
AFS-BR-09	AFS-06-B	0.3	NA	74.9	36.9	116	0.71	-11.2	0.05	NA
AFS-BR-10	AFS-02-A	0.0	NA	74.8	40.2	114	0.65	-10.2	0.05	NA
AFS-BR-11	AFS-06-G	0.7	NA	75.0	38.9	246	1.43	-9.4	0.05	NA
AFS-BR-12	AFS-06-F	0.7	4.6	75.2	37.2	227	1.37	-10.0	0.50	1.05
AFS-BR-13	AFS-07-F	0.5	NA	74.9	37.4	262	1.59	-26.1	0.05	NA
AFS-BR-14	AFS-07-A	0.0	5.8	74.9	38.9	163	0.95	-26.1	0.05	1.27
AFS-BR-15	AFS-06-D	0.6	6.3	75.1	38.8	183	1.06	-26.2	0.05	1.38
AFS-BR-16	AFS-03-H	0.9	7.3	75.3	39.4	231	1.32	-26.4	0.05	1.57
AFS-BR-17	AFS-01-B	0.1	4.5	73.9	41.0	167	0.95	-26.3	0.05	0.95

P_{br} -peak diametral load

T_{br}-Brazilian tensile strength

T_{br} (MPa) = $2 \times P_{br}$ (N) / $[\pi \times \text{Diameter(mm)} \times \text{Thickness(mm)}]$

NA – not available

4.3 Unconfined uniaxial compression tests

Uniaxial compression tests were conducted in a 0.1 MN servo-controlled loading machine. The prepared specimens were loaded at a constant displacement rate of 10^{-3} mm/s which corresponds to a strain rate of 10^{-5} /s. The axial and lateral deformations were measured from the axial and the circumferential LVDT's, respectively. The instrumented specimen was placed between the upper and lower cylindrical end-caps with the same diameter as the specimen. The specimens were loaded until 5 to 6% of axial strain was reached. Unlike the brittle failure observed in the rock, the frozen soil specimens were deformed in a ductile manner, without the peak stress and significant stress drop immediately following it. Therefore, the uniaxial compressive strength of the frozen soil was not calculated. Instead of the uniaxial compressive strength, dilatancy was considered to be the measure of damage stress for the frozen soil. The dilatancy, defined as the point at which the specimen reaches its minimum volume, was based on the volumetic strain, ε_v, calculated as follows:

$$\varepsilon_v = \varepsilon_a + 2\varepsilon_l$$

where ε_a and ε_l are the axial and lateral strains, respectively.

Based on the volumetric strain data, dilatancy was observed in two uniaxial compression tests: (AFS-UC-04 and AFS-UC-09).

The proportional constant between stress and strain in the elastic portion of compression tests defines the Young's modulus:

$$E = \sigma_a / \varepsilon_a$$

where σ_a is the axial stress and ε_a is the axial strain. The Young's modulus was determined by fitting a straight line (or linear regression analysis) to the stress strain data that ranged from approximately 10 to 50% of the peak stress. When approximately 50% of the expected peak load P was reached, unloading and reloading cycles were carried out. The elastic Young's modulus, $E_{elastic}$, due only to the elastic deformation of the specimen, was calculated from the slope of the unloading curve. Linear regression analysis was also used to obtain the best-fit straight line to the unloading curve.

Also, the ratio between the axial (ε_a) and lateral (ε_l) strains is defined as the Poisson's ratio (ν):

$$\nu = |\varepsilon_l| / |\varepsilon_a|$$

Nine Alaskan frozen soil specimens were tested to obtain elastic constants, E, $E_{elastic}$ and ν. The results are summarized in Table 5. Figure 19 shows the example of unloading and reloading cycles for the uniaxial compression test. The onset of dilatancy for the same test is shown in Figure 20.

The variations of $E_{elastic}$, with respect to the depth, density and temperature of the Alaskan frozen soil are shown in Figure 21. In order to correlate $E_{elastic}$ to different test variables, we grouped the test results, with respect to the set temperature, in the frozen soil. Solid symbols in Figure 21

represent $E_{elastic}$ results of the frozen soil obtained at approximately -10ºC. Because of the inhomogeneity of the frozen soil, $E_{elastic}$ varies in wide ranges. However, it appears that $E_{elastic}$ increases with the density and the depth of the soil and decreases with the temperature. The Poisson's ratio for the frozen soil ranges from 0.006 to 0.13. These values were calculated in the elastic region and were relatively small compared to other geomaterials (i.e. 0.25 for the rock).

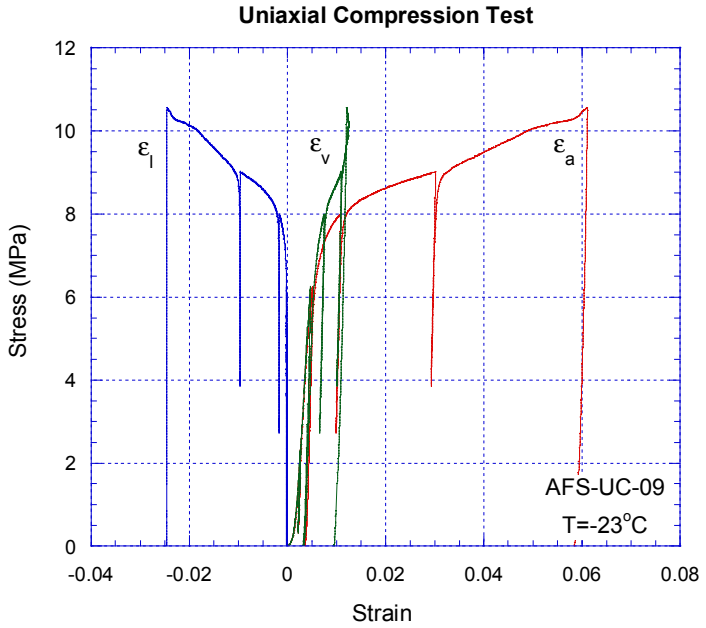

Figure 19. Stress-strain plot for the AFS-UC-09 uniaxial compression test. Shown are the axial strain (ε_a); lateral strain (ε_l); and volumetric strain (ε_v).

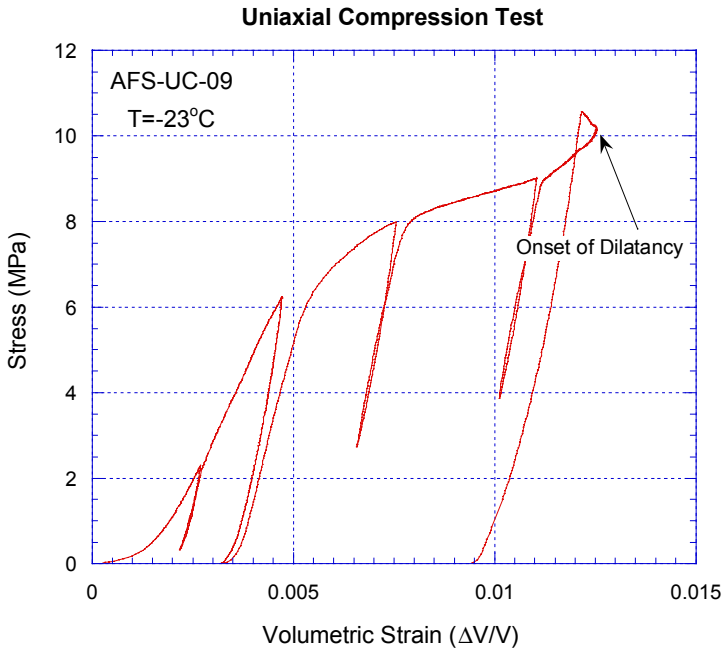

Figure 20. Stress-volumetric strain plot for the AFS-UC-09 uniaxial compression test showing the onset of dilatancy.

Table 5. Summary of uniaxial compression tests of Alaskan frozen soil.

Test No.	Sample Location	Depth	Diameter	Length	Weight	Density	Temperature	$\sigma_{a,d}$	$E_{elastic}$			E	ν
									$cycle_a$	$cycle_b$	$cycle_c$		
		(m)	(mm)	(mm)	(g)	(g/cm^3)	(ºC)			(GPa)		(GPa)	
AFS-UC-01	NA	NA	44.5	100.3	NA	NA	-10.7	NA	2.6	3.4	3.7	1.1	NA
AFS-UC-02	AFS-03-D	0.4	44.5	99.6	NA	NA	-9.6	NA	0.7	0.6	0.6	0.1	NA
AFS-UC-03	AFS-11-D	0.5	44.2	100.1	217	1.42	-10.5	NA	1.7	NA	NA	0.5	NA
AFS-UC-04	AFS-12-D	0.6	44.5	103.4	NA	NA	-10.2	4.0	1.4	1.3	1.2	0.5	0.006
AFS-UC-05	AFS-12-A	0.2	44.2	101.1	125	0.81	-9.8	NA	0.8	0.6	0.8	0.3	NA
AFS-UC-06	AFS-15-H	0.8	44.5	100.1	263	1.69	-5.1	NA	1.3	1.7	2.5	1.9	0.128
AFS-UC-07	AFS-13-C	0.3	43.9	103.1	104	0.66	-24.7	NA	0.7	0.6	0.6	0.4	NA
AFS-UC-08	AFS-13-E	0.7	44.5	100.8	210	1.34	-4.7	NA	1.2	0.7	0.5	0.3	0.018
AFS-UC-09	AFS-08-H	0.7	44.2	99.8	244	1.59	-23.1	10.1	3.7	4.8	4.8	1.2	0.016

$\sigma_{a,d}$ - dilation limit (psi)

$E_{elastic}$ - Elastic Young's modulus obtained from the slope of the unloading and reloading curves.

E (Young's Modulus)= σ_a / ε_a (psi)

$cycle_a$ to $cycle_c$ - unloading and reloading cycles selected for the calculation of $E_{elastic}$

ν (Poisson's ratio) = $| \varepsilon_l | / | \varepsilon_a |$

NA: not available

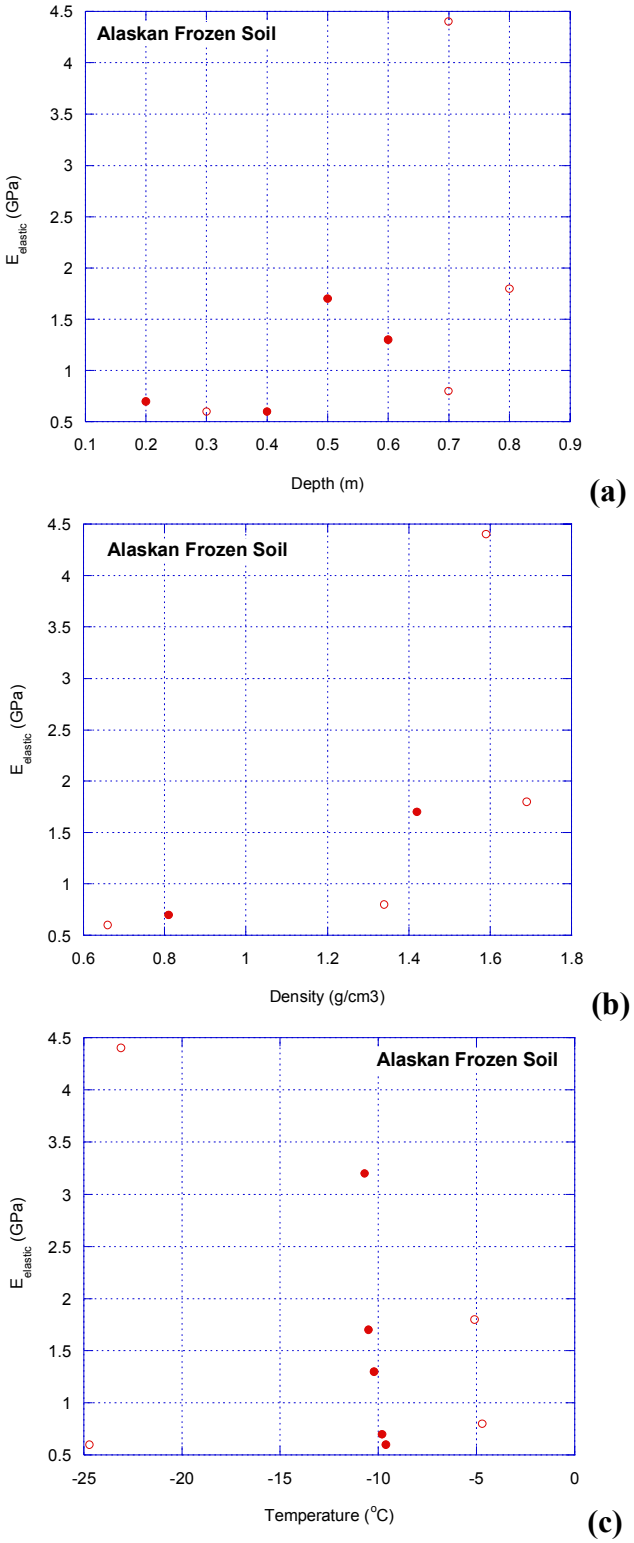

Figure 21. Effects of **(a)** depth **(b)** density and **(c)** temperature on the elastic Young's modulus ($E_{elastic}$) of Alaskan frozen soil. Solid data points measured from approximately the same temperature of around -10ºC.

4.4 Triaxial compression tests

To populate the necessary database for the deformational behavior of the Alaskan frozen soil under deviatoric stress conditions ($\sigma_1>\sigma_2=\sigma_3=P$), a series of triaxial tests was conducted under different temperatures and confining pressure conditions. The sample preparation procedures and test equipment for the triaxial tests were identical to those used for the hydrostatic compression tests.

After the specimen assembly was placed in the HPLT vessel, hydraulic pressure was applied to a predetermined level of confining pressure. The servo-controller maintained the pressure level ($\sigma_1=\sigma_2=\sigma_3=P$; where σ_1, σ_2, and σ_3 are the maximum, intermediate and minimum principal stresses, respectively). After the confining pressure, P, was stabilized, the specimen was loaded axially at a constant axial strain rate of 10^{-5} /s to create the deviatoric stress condition.

The confining pressure was measured with a pressure transducer connected to the HPLT vessel and the axial and lateral displacements were measured with the internal LVDT's (see Figure 7). The triaxial compression test followed the loading path C or D in I_1 vs. $\sqrt{J_2}$ plot shown in Figure 1. The test conditions and the results are summarized in Table 6.

Figure 22 shows a typical plot obtained from a triaxial compression test of a frozen soil specimen. The stress-strain plot shows the onset of dilatancy (or dilation limit) around 6.5 MPa of σ_c-P. At this stress level, the material reaches its minimum volume.

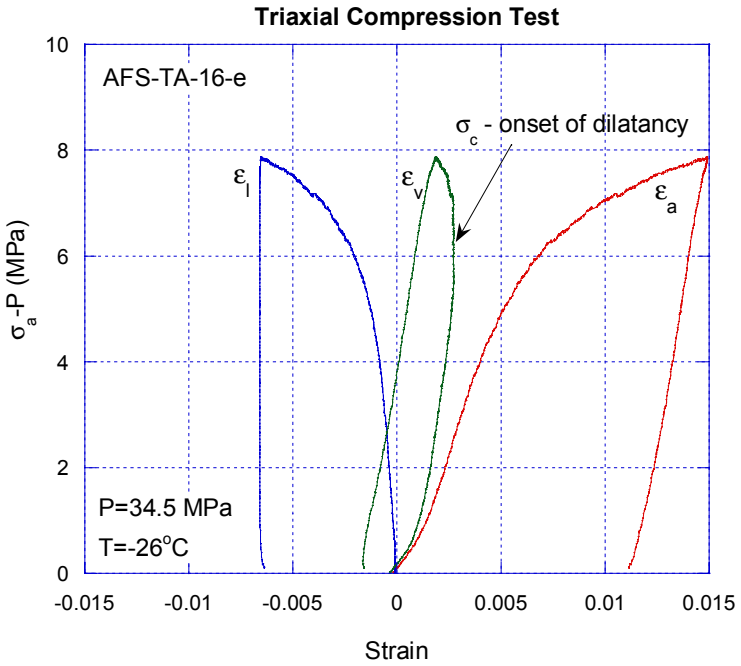

Figure 22. Stress-strain plot for the AFS-TA-16-e triaxial compression test. Shown are the axial strain (ε_a); lateral strain (ε_l); and volumetric strain (ε_v).

Table 6. Summary of triaxial compression tests of Alaskan frozen soil.

Test No.	Sample Location	Depth (m)	Diameter (mm)	Length (mm)	Weight (g)	Density (g/cm^3)	T (°C)	P (MPa)	σ_c-P (MPa)	σ_c (MPa)	E (GPa)	$E_{elastic}$ (GPa)	I_1 (MPa)	$J_2^{0.5}$ (MPa)
AFS-TA-01-a	AFS-10-F	0.7	44.3	97.5	240	1.59	-10	6.9	4.4	11.3	0.4		25.1	2.5
AFS-TA-01-b	AFS-10-F	0.7	44.3	97.5	240	1.59	-9	13.8	4.3	18.1	1.4		45.7	2.5
AFS-TA-02	AFS-09-C	0.6	43.8	101.1	230	1.51	-10	13.8	4.7	18.5	1.3		46.1	2.7
AFS-TA-03	AFS-10-E	0.6	43.9	99.6	223	1.47	-10	20.7	5.2	25.9	2.4		67.3	3.0
AFS-TA-04	AFS-09-B	0.4	44.2	102.2	244	1.56	-10	27.2	4.2	31.4	0.8		85.7	2.4
AFS-TA-05	AFS-04-A	0.1	44.1	102.0	177	1.13	-10	20.7	4.5	25.2	1.0		66.6	2.6
AFS-TA-06-a	AFS-14-E	0.6	44.5	102.4	NA	NA	-10	3.4	4.7	8.1	0.5		15.0	2.7
AFS-TA-06-b	AFS-14-E	0.6	44.5	102.4	NA	NA	-10	27.6	4.4	32.0	0.7		87.2	2.5
AFS-TA-06-c	AFS-14-E	0.6	44.5	102.4	NA	NA	-10	24.1	5.1	29.2	2.1		77.5	2.9
AFS-TA-06-d	AFS-14-E	0.6	44.5	102.4	NA	NA	-10	20.7	4.6	25.3	2.3		66.7	2.7
AFS-TA-06-e	AFS-14-E	0.6	44.5	102.4	NA	NA	-10	17.2	5.9	23.1	2.3		57.6	3.4
AFS-TA-07-a	AFS-15-C	0.3	43.9	101.1	NA	NA	-10	0.7	3.9	4.6	1.6		6.0	2.3
AFS-TA-07-b	AFS-15-C	0.3	43.9	101.1	NA	NA	-10	3.4	9.0	12.4	2.1	3.5	19.3	5.2
AFS-TA-07-c	AFS-15-C	0.3	43.9	101.1	NA	NA	-10	6.9	4.4	11.3	1.6		25.1	2.5
AFS-TA-07-d	AFS-15-C	0.3	43.9	101.1	NA	NA	-10	13.8	4.6	18.4	1.5		46.0	2.7
AFS-TA-07-e	AFS-15-C	0.3	43.9	101.1	NA	NA	-10	17.2	4.8	22.0	2.8		56.5	2.8
AFS-TA-07-f	AFS-15-C	0.3	43.9	101.1	NA	NA	-10	24.1	4.9	29.0	2.5		77.3	2.8
AFS-TA-08	AFS-13-D	0.5	44.3	101.7	188	1.20	-11	3.4	2.4	5.8	NA		12.7	1.4
AFS-TA-09-a	AFS-13-D	0.5	44.3	101.7	188	1.20	-10	6.9	NA	NA	0.4		NA	NA
AFS-TA-09-b	AFS-13-D	0.5	44.3	101.7	188	1.20	-10	13.8	3.5	17.3	0.6		44.9	2.0
AFS-TA-09-c	AFS-13-D	0.5	44.3	101.7	188	1.20	-10	20.7	3.0	23.7	1.2		65.1	1.7
AFS-TA-09-d	AFS-13-D	0.5	44.3	101.7	188	1.20	-10	41.4	2.8	44.2	1.3		126.9	1.6
AFS-TA-10	AFS-15-B	0.2	44.2	101.2	250	1.61	-25	3.3	10.4	13.7	1.3		20.4	6.0
AFS-TA-11-a	AFS-15-B	0.2	44.2	101.2	250	1.61	-25	13.8	9.9	23.7	2.7		51.3	5.7
AFS-TA-11-b	AFS-15-B	0.2	44.2	101.2	250	1.61	-25	20.7	10.6	31.3	4.0		72.7	6.1

(Continued on the next page.)

Table 6. Summary of triaxial compression tests of Alaskan frozen soil (Continued).

Test	Sample	Depth	Diameter	Length	Weight	Density	T	P	σ_c-P	σ_c	E	$E_{elastic}$	I_1	$J_2^{0.5}$

No.	Location												
		(m)	(mm)	(mm)	(g)	(g/cm^3)	(°C)	(MPa)	(MPa)	(MPa)	(GPa)	(GPa)	(MPa)	(MPa)
AFS-TA-11-c	AFS-15-B	0.2	44.2	101.2	250	1.61	-25	41.0	10.6	51.6	4.1		133.5	6.1
AFS-TA-12	AFS-13-A	0.1	44.3	98.9	111	0.72	-5	3.3	NA	NA	NA		NA	NA
AFS-TA-13-a	AFS-14-C	0.4	44.2	103.1	196	1.24	-6	3.4	NA	NA	0.1		NA	NA
AFS-TA-13-b	AFS-14-C	0.4	44.2	103.1	196	1.24	-6	6.9	NA	NA	0.3		NA	NA
AFS-TA-13-c	AFS-14-C	0.4	44.2	103.1	196	1.24	-6	13.8	1.2	15.0	0.3		42.6	0.7
AFS-TA-13-d	AFS-14-C	0.4	44.2	103.1	196	1.24	-6	20.7	NA	NA	0.3		NA	NA
AFS-TA-14-a	AFS-12-C	0.4	44.2	102.1	232	1.48	-26	3.4	NA	NA	2.0	3.5	NA	NA
AFS-TA-14-b	AFS-12-C	0.4	44.2	102.1	232	1.48	-26	13.8	NA	NA	3.1		NA	NA
AFS-TA-14-c	AFS-12-C	0.4	44.2	102.1	232	1.48	-26	20.7	NA	NA	3.1		NA	NA
AFS-TA-14-d	AFS-12-C	0.4	44.2	102.1	232	1.48	-26	34.0	8.9	42.9	3.2		110.8	5.1
AFS-TA-14-e	AFS-12-C	0.4	44.2	102.1	232	1.48	-26	54.6	8.5	63.1	3.7		172.2	4.9
AFS-TA-15-a	AFS-15-G	0.7	44.2	100.6	240	1.56	-6	1.0	NA	NA	0.5	1.3	NA	NA
AFS-TA-15-b	AFS-15-G	0.7	44.2	100.6	240	1.56	-6	3.4	NA	NA	0.8	1.5	NA	NA
AFS-TA-15-c	AFS-15-G	0.7	44.2	100.6	240	1.56	-6	6.9	NA	NA	0.5		NA	NA
AFS-TA-15-d	AFS-15-G	0.7	44.2	100.6	240	1.56	-6	13.8	1.6	15.4	0.6		43.0	0.9
AFS-TA-16-a	AFS-14-A	0.2	44.1	100.6	146	0.95	-26	1.6	NA	NA	1.1		NA	NA
AFS-TA-16-b	AFS-14-A	0.2	44.1	100.6	146	0.95	-26	3.4	NA	NA	1.6		NA	NA
AFS-TA-16-c	AFS-14-A	0.2	44.1	100.6	146	0.95	-26	7.2	NA	NA	1.3		NA	NA
AFS-TA-16-d	AFS-14-A	0.2	44.1	100.6	146	0.95	-26	13.8	NA	NA	1.2		NA	NA
AFS-TA-16-e	AFS-14-A	0.2	44.1	100.6	146	0.95	-26	34.5	6.5	41.0	1.2		109.9	3.8

σ_c - Critical stress (MPa) obtained at the stress level for dilation limit or 2 % axial strain.

$E_{elastic}$ - Elastic Young's modulus obtained from the slope of the unloading and reloading curves.

E (Young's Modulus)= σ_a / ε_a ; P-confining pressure ; T-Temperature

ν (Poisson's ratio) = $| \varepsilon_l | / | \varepsilon_a |$

$I_1 = \sigma_1+2P$; ; $J_2^{0.5}=(\sigma_1-P) / (3^{0.5})$

NA: not available

4.5 Quasi-dynamic unconfined uniaxial compression tests

A series of uniaxial compression tests was performed using quasi-dynamic strain rate (approximately 10 /s), generated by the stroke control of the 0.1 MN loading machine in the environmental chamber (Figure 15). The quasi-dynamic compression tests serve to bridge the gap in strain rates used for the quasi-static (10^{-5} /s range) and the SHPB (10^{3} /s) compression tests. Right cylindrical disk specimens were prepared to have nominal dimensions of 25 mm in diameter and 113 mm in thickness. The dimensions of the specimens were similar to those used for the SHPB tests. The prepared specimens were kept in the environmental chamber under set temperature (-5 or –25°C) for over an hour before testing to achieve uniform temperatures in the frozen soil specimens. The push rod of the loading machine was set to travel at 100 mm/s, yielding a strain rate of approximately 10 /s. The load was measured by the load cell and the axial deformation was measured by the stroke of the loading machine.

Figure 23 shows the stress-strain plots obtained at -5ºC under quasi-dynamic compression tests. Figure 24 shows the stress-strain plots obtained at a relatively lower temperature of -25ºC. As shown in Figure 25, we were able to accomplish constant strain rate represented as the constant slope of the strain-time plots between 7.5 to 9 s^{-1}. Table 7 summarizes the results from 18 quasi-dynamic compression tests conducted at two temperatures (–25 and -5°).

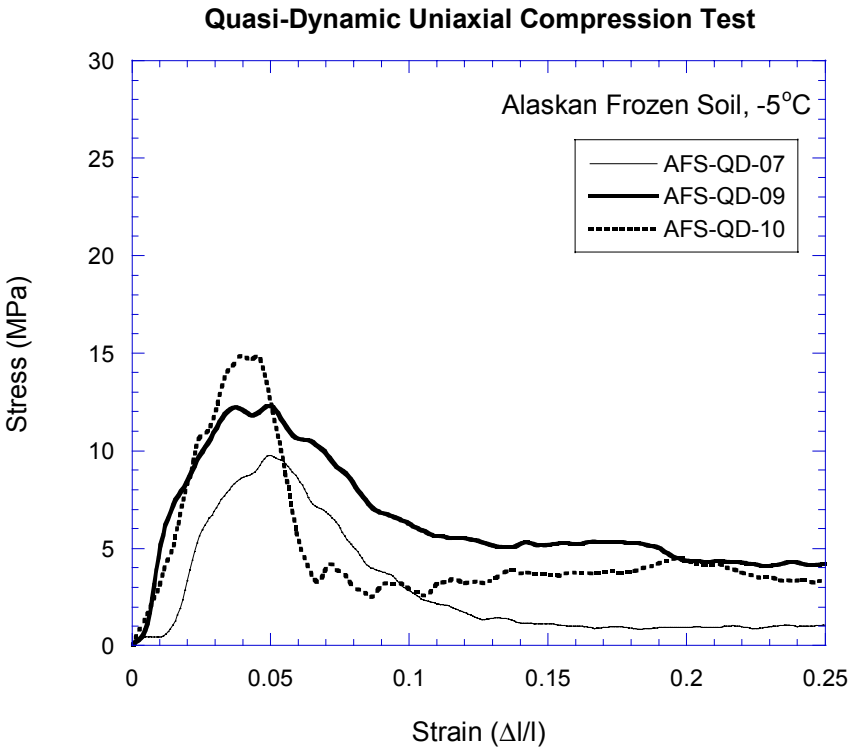

Figure 23. Typical stress-strain records obtained during the quasi-dynamic uniaxial compression tests for the Alaskan Frozen Soil (AFS) specimens at –5ºC.

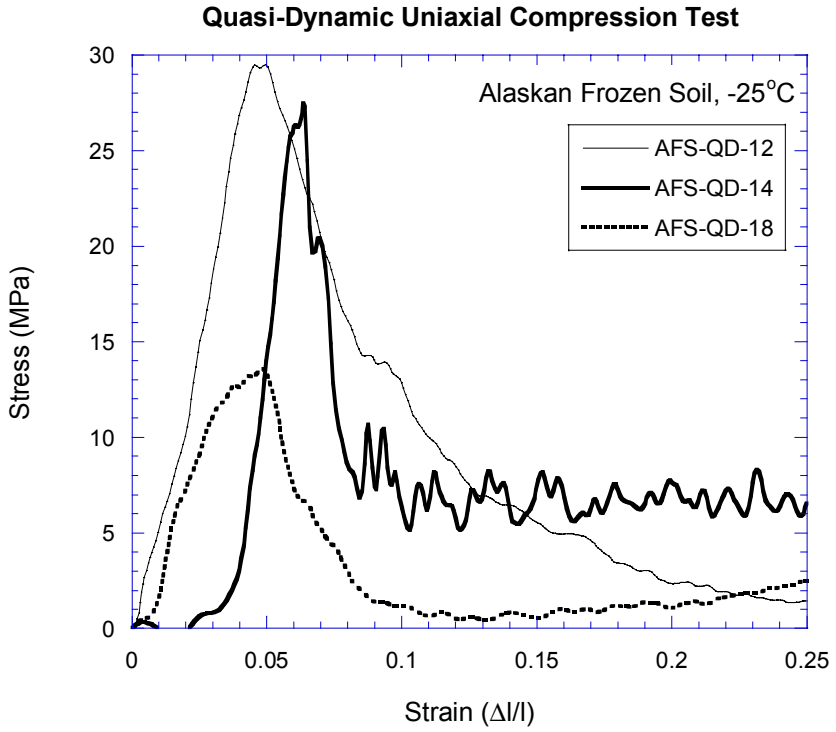

Figure 24. Typical stress-strain records obtained during the quasi-dynamic uniaxial compression tests for the Alaskan Frozen Soil (AFS) specimens at –25ºC.

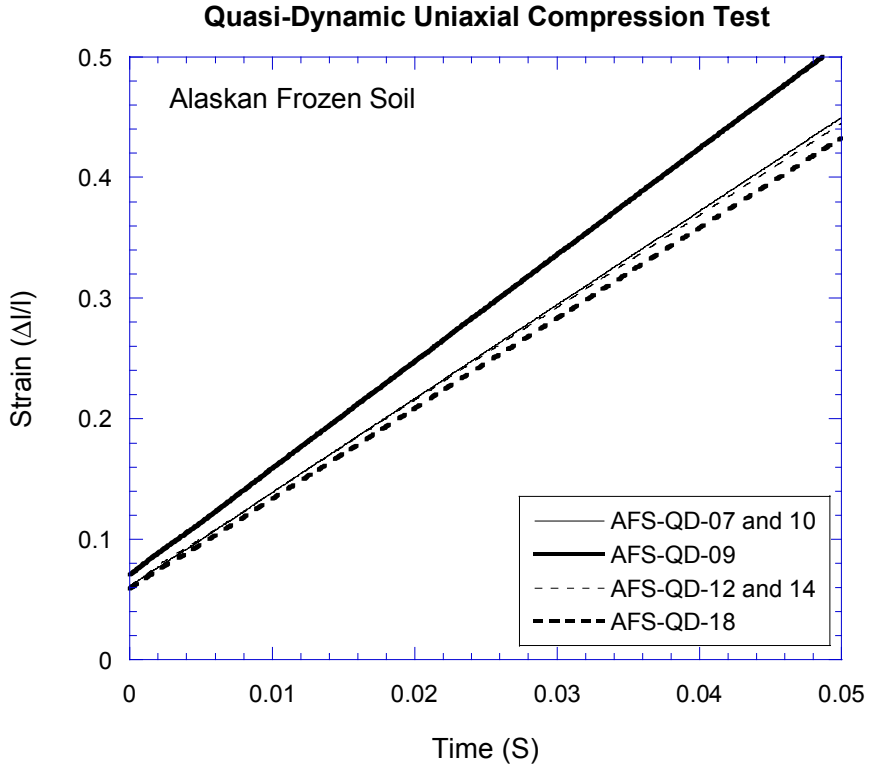

Figure 25. Typical strain-time records obtained during the quasi-dynamic uniaxial compression tests for the Alaskan Frozen Soil (AFS) specimens.

The quasi-dynamic compressive strength of the frozen soil at -5°C is determined to be 10.5 (±1.2) MPa without the result from the low density (0.94 g/cm^3) specimen AFS-QD-15. The Young's modulus varied from 210 to 450 MPa. The quasi-dynamic compressive strength of the frozen soil at -25°C is determined to be 21.8 (±6.4) MPa, excluding the result from the low density specimen AFS-QD-06 (0.92 g/cm^3). The Young's modulus varied widely from 280 to 1,120 MPa. As shown in Figure 26, the strength and the Young's modulus of the frozen soil, generally increase with density. Figure 27 shows that the low temperature setting will make the frozen soil more rigid with higher strength and higher Young's modulus.

Table 7. Summary of quasi-dynamic uniaxial compression tests of Alaskan frozen soil .

Specimen No.	Diameter (cm)	Length (cm)	Weight (g)	Temperature (^{o}C)	Density (g/cm^3)	Strain Rate* (s^{-1})	C_0 (MPa)	Young's Modulus (MPa)
AFS-QD-01	2.59	1.26	4.30	NA	0.65	8.0	2.4	40
AFS-QD-02	2.59	1.00	3.21	NA	0.61	9.9	3.6	10
AFS-QD-03	2.57	1.19	9.47	NA	1.53	8.4	14.6	660
AFS-QD-04	2.57	1.13	8.53	NA	1.46	8.9	6.5	130
AFS-QD-05	2.18	1.27	5.88	-5	1.24	8.0	9.8	360
AFS-QD-06	2.16	1.30	4.48	-5	0.94	7.8	5.9	270
AFS-QD-07	2.24	1.30	6.59	-5	1.30	7.8	9.7	450
AFS-QD-08	2.13	1.27	6.42	-5	1.41	7.8	10.3	310
AFS-QD-09	2.16	1.14	6.36	-5	1.52	8.0	12.3	360
AFS-QD-10	2.26	1.30	7.01	-5	1.35	7.8	14.9	380
AFS-QD-11	2.24	1.19	7.35	-5	1.57	8.5	10.4	210
AFS-QD-12	2.24	1.32	8.61	-25	1.66	7.7	29.5	700
AFS-QD-13	2.13	1.35	7.07	-25	1.47	7.5	20.2	NA**
AFS-QD-14	2.26	1.32	7.12	-25	1.34	7.7	27.5	1120
AFS-QD-15	2.18	1.30	4.45	-25	0.92	7.8	8.1	280
AFS-QD-16	2.18	1.32	5.75	-25	1.16	7.7	16.4	NA**
AFS-QD-17	2.21	1.19	6.25	-25	1.37	8.5	15.4	490
AFS-QD-18	2.18	1.35	6.35	-25	1.26	7.5	13.6	460

C_0 - Uniaxial compressive strength

*-Stroke control 100 mm/s was used to generate the strain rate.

NA- Not Available

NA**- The ascending portion of the stress-strain curve was missing due to a late trigger.

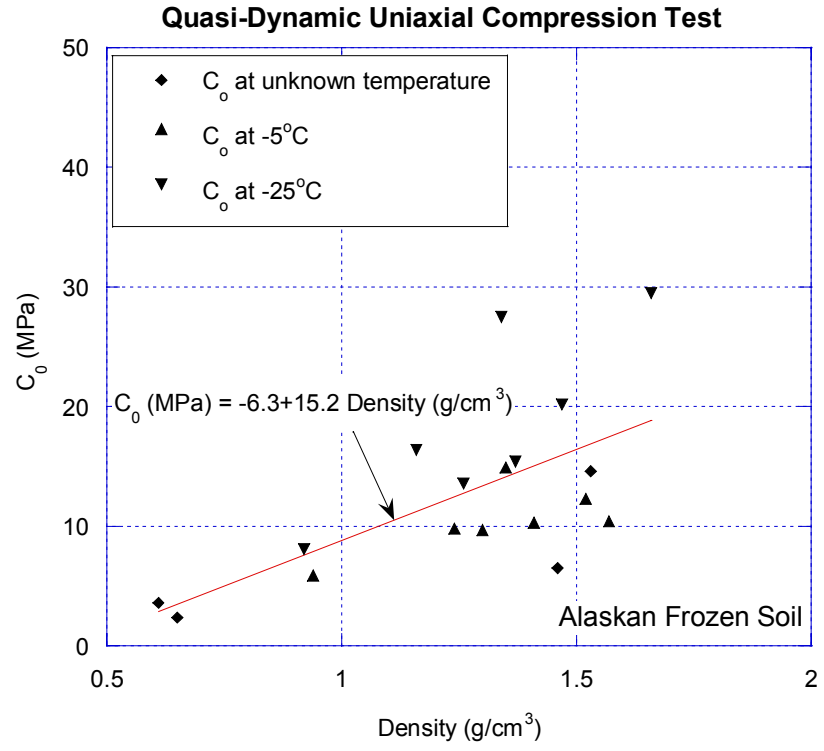

(a)

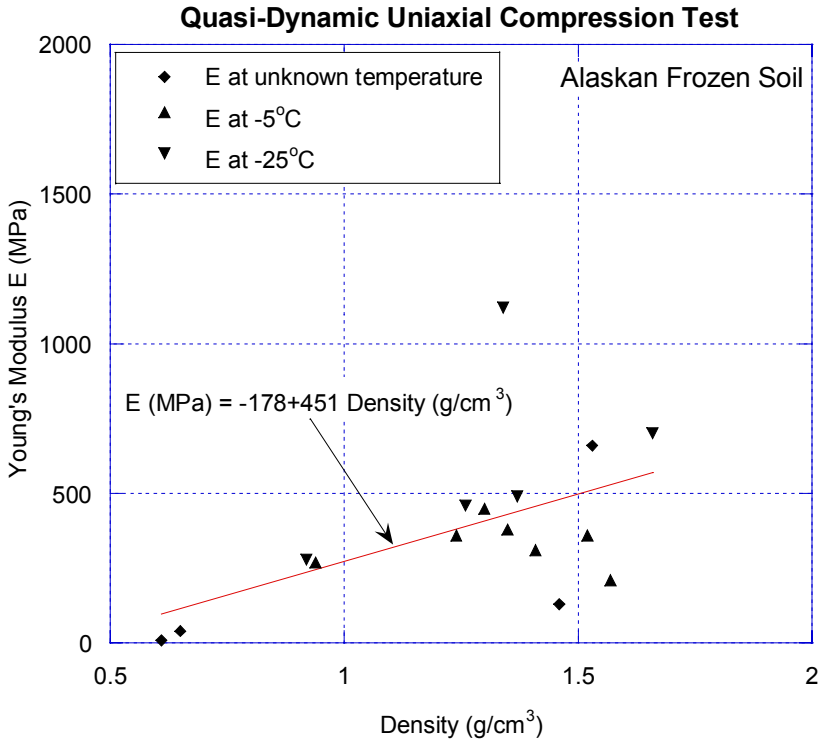

(b)

Figure 26. Effects of density on **(a)** the uniaxial compressive strength (C_0) and **(b)** the Young's modulus (E) of Alaskan frozen soil.

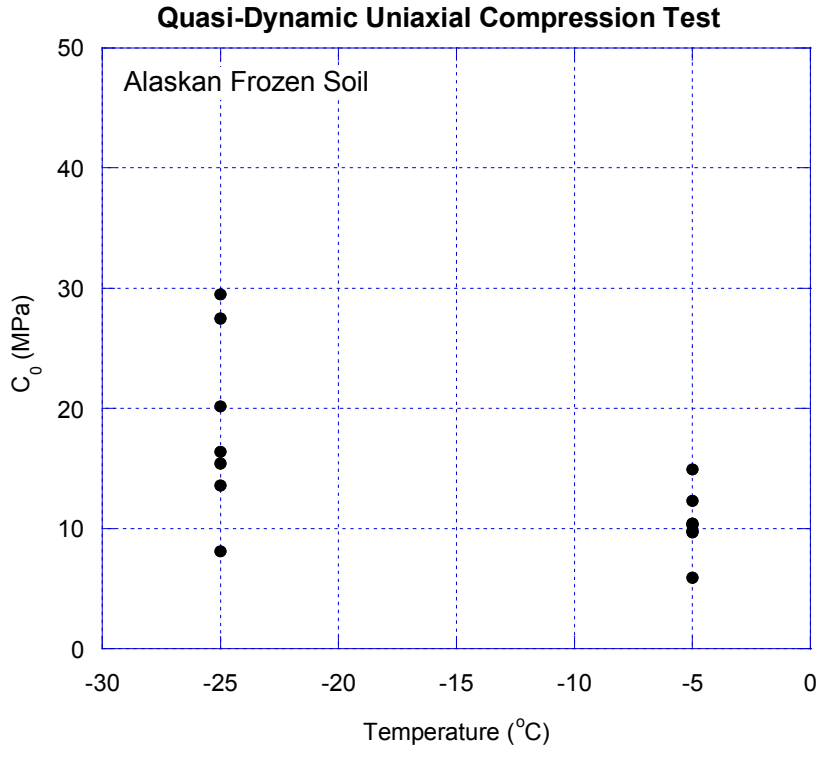

(a)

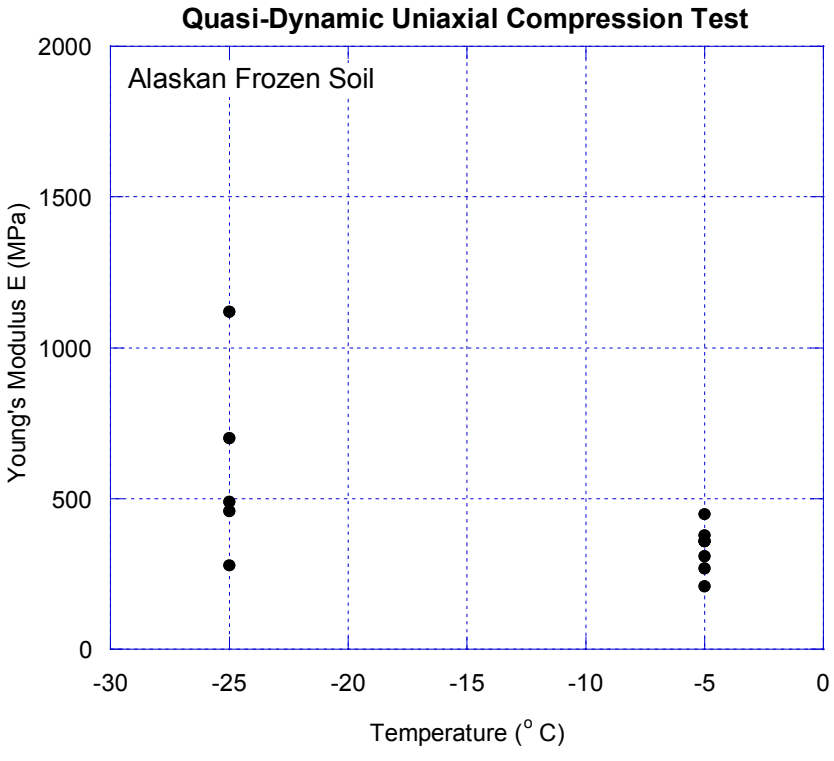

(b)

Figure 27. Effects of temperature on **(a)** the uniaxial compressive strength (C_0) and **(b)** the Young's modulus (E) of Alaskan frozen soil.

4.6 Split Hopkinson pressure bar (SHPB) tests

Experimental set-up

To investigate the dynamic behavior of frozen soil under compression, the split Hopkinson pressure bar (SHPB) was used (Kolsky, 1949). Figures 28 and 29 show the schematic and the picture of the SHPB set-up used for testing the Alaskan frozen soil. The SHPB set-up was composed of a striker bar, an incident bar and a transmission bar. The incident and the transmission bars were instrumented with strain gages to capture elastic waves generated by the striker bar. A frozen soil sample was placed between the incident and the transmission bars and the striker bar was launched by compressed air. An oscilloscopic fast data acquisition system captured the wavelets in the incident and the transmission bars at a rate of 5 million sample/s per channel. A low temperature enclosure was designed to enclose a frozen soil specimen under constant freezing temperature while testing the specimen.

The elastic compression wave was generated by impacting the striker bar into the incident bar. The pressure wave was transmitted through the specimen and partially reflected at the interface between the specimen and the incident bar, if the impedance of the specimen is less than that of the bars. Because of the low acoustic impedance of the frozen soil, the reflected and transmitted signals registered to strain gages have low signal to noise ratio. To increase the signal to noise ratio, 7075-T6 Aluminum was used as the material for the incident and transmission bars and the high output semiconductor strain gages were used to measure pressure waves.

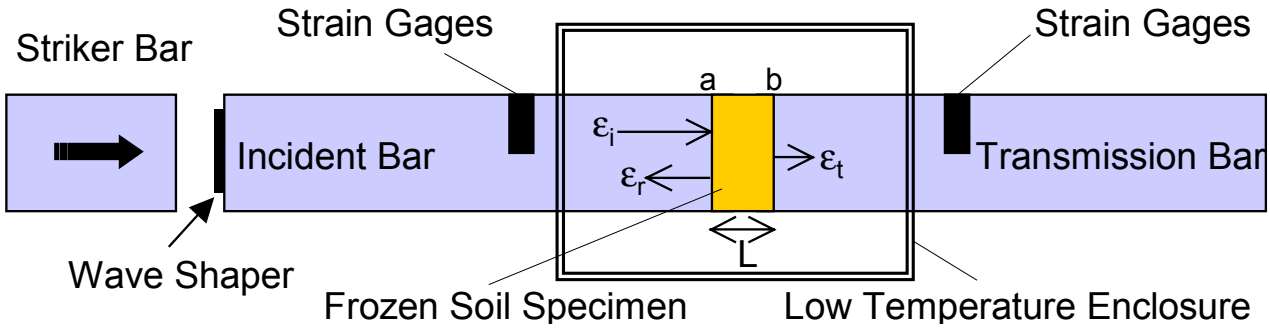

Figure 28. Schematic of the SHPB system used for testing Alaskan frozen soil.

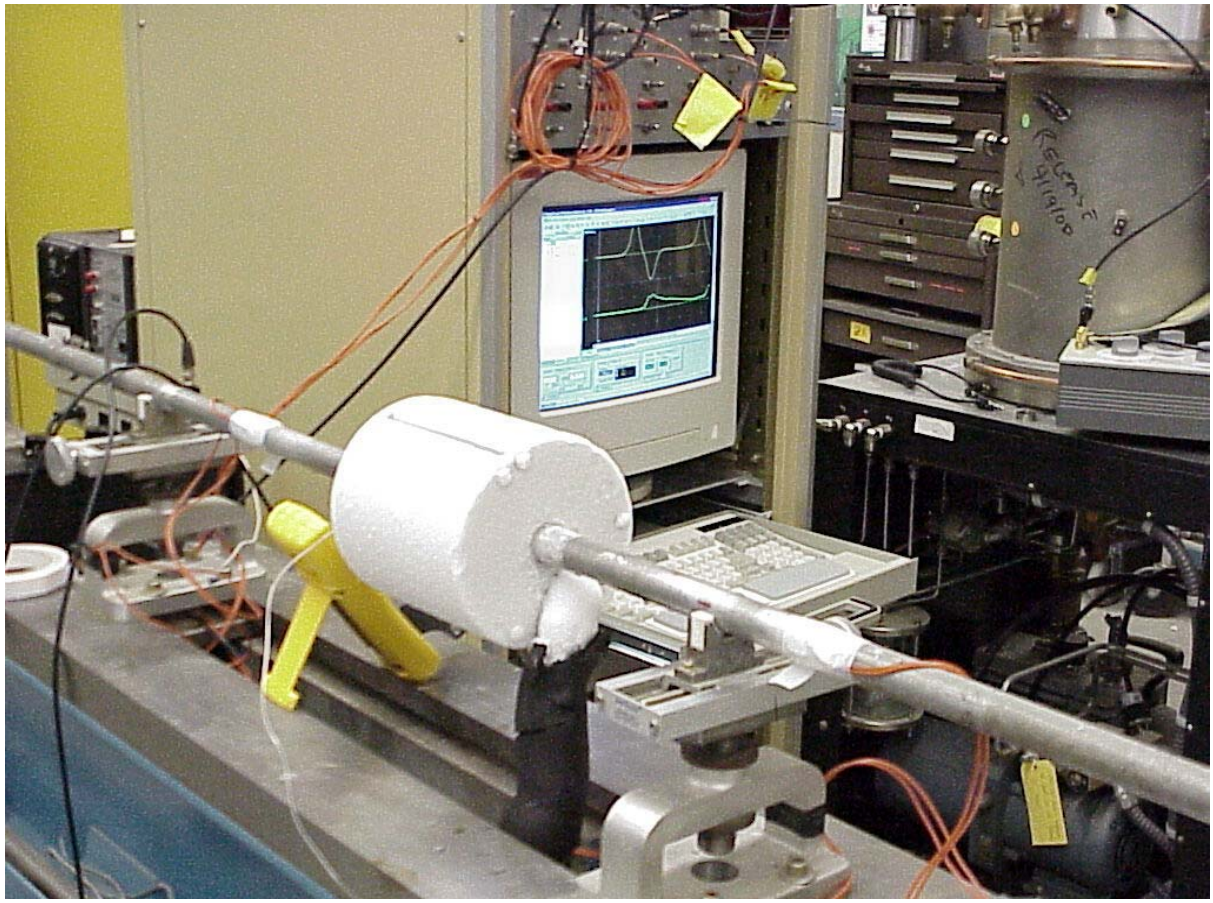

Figure 29. The SHPB testing system used for testing Alaskan frozen soil.

Theory of the SHPB testing

When the striker bar impacts the incident bar, an elastic wave is generated and travels through the incident bar. When the elastic wave reached the interface between the incident bar and the specimen, a fraction of the wave is reflected back into the incident bar due to the impedance mismatch between the sample and the bar. The remainder of the wave travels through the specimen and reaches the interface between the specimen and the transmission bar. Based on one dimensional theory of elastic wave propagation in a bar and the continuity of displacement and stress equilibrium at the interface, the following equations can be derived to describe stress, strain and strain rate in the specimen (Kolsky, 1949; Lindholm, 1964):

$$\sigma_a = E\frac{A}{A_s}(\varepsilon_i + \varepsilon_r)$$

$$\sigma_b = E\frac{A}{A_s}(\varepsilon_t)$$

$$\dot{\varepsilon} = -\frac{2C_0}{L}\varepsilon_r$$

$$\varepsilon = \frac{2C_0}{L}\int_0^t \varepsilon_r dt$$

where σ_a is the stress in the interface between the sample and the incident bar; σ_b is the stress in the interface between the sample and the transmission bar; E is the modulus of the transmission bar (72 GPa for 7075-T6 Aluminum); A is the cross-sectional area of the transmission bar; A_s is the cross-sectional area of the specimen; ε_i, ε_r, and ε_t are the incident, reflected, and transmitted strains, respectively (see Figure 28); $\dot{\varepsilon}$ is the strain rate in the specimen; C_0 is the longitudinal wave velocity in the incident bar; L is the initial length of the specimen; and t is time.

If the material is very weak, it does not have the stiffness to transmit the high-amplitude loading on the incident-bar interface through the specimen length effectively. As a result, the portion of the specimen near the interface close to the incident bar, gets compacted and pushed quickly towards the transmitter interface. This compacted section of the specimen experiences large axial acceleration. The stress on the incident-bar interface needs to overcome the inertia induced by this large acceleration. On the other hand, the transmission bar interface does not "feel" this acceleration, due to the low strength and low wave speed in the unpacked portion of the specimen. Therefore, the difference between the two stresses σ_a and σ_b will be large for weak materials.

To achieve an equilibrated stress state and homogeneous deformation throughout the specimen, the load at the incident-bar interface should rise gradually through pulse shaping. Detailed discussion on stress equilibrium and homogeneous deformation by pulse shaping can be found in Frew et. al.(2002).

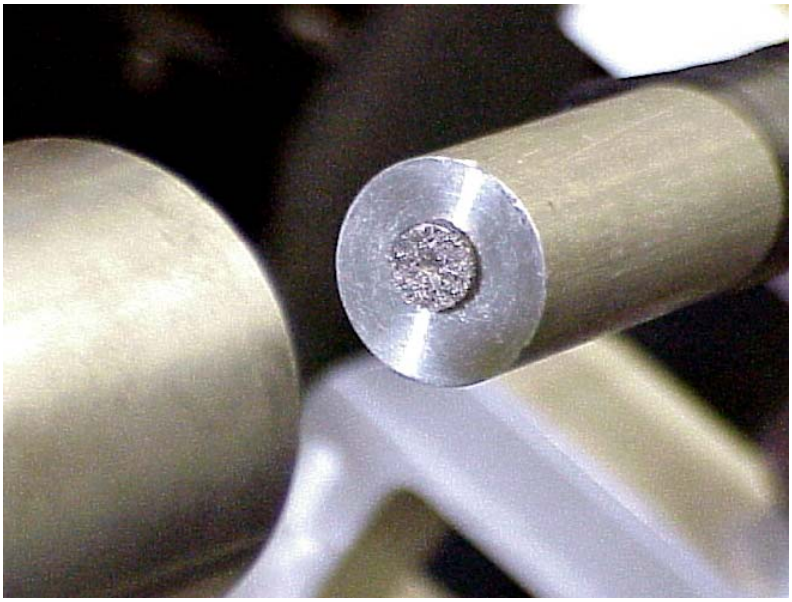

Figure 30. Felt metal disk, approximately 1 cm in diameter and 0.2 cm in thickness, used as a pulse shaper.

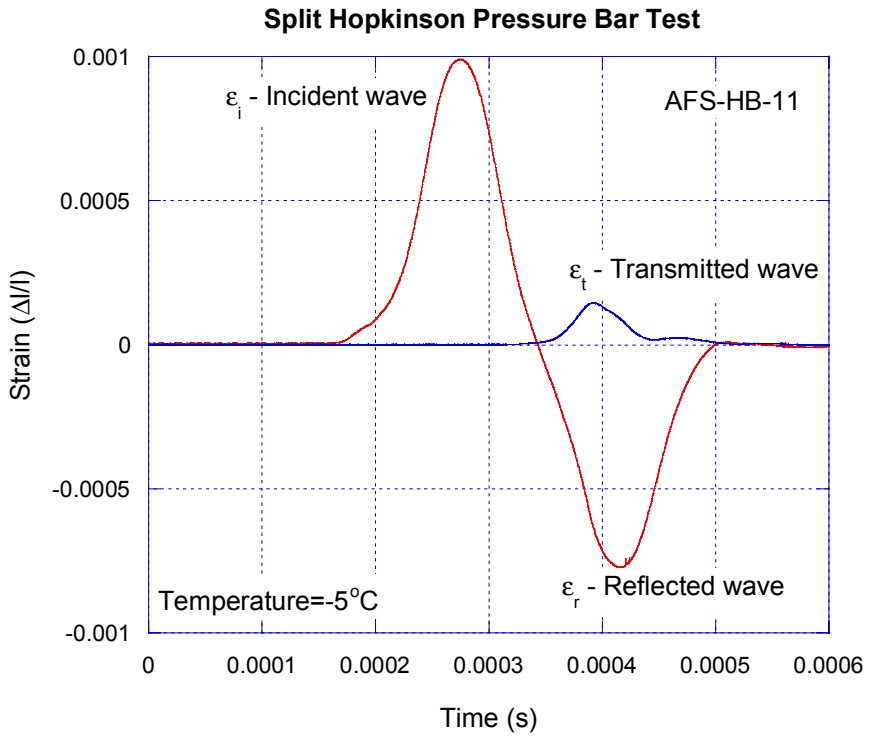

Figure 31. Typical strain-time record obtained during SHPB testing of an Alaskan frozen soil specimen.

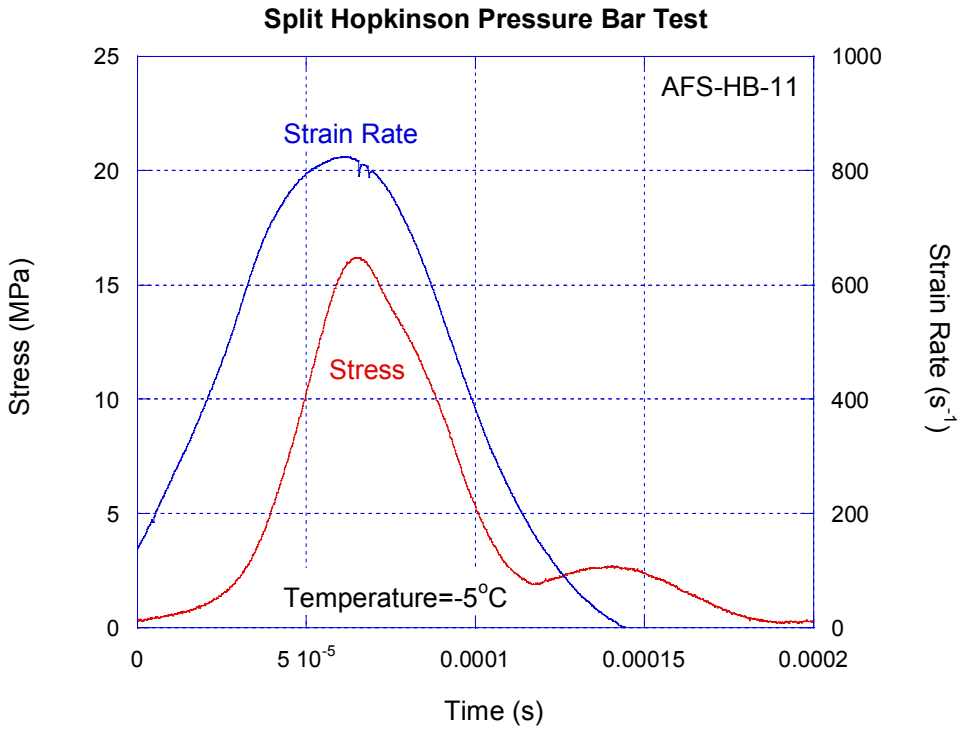

Figure 32. Typical stress-time and strain rate-time record obtained during SHPB testing of an Alaskan frozen soil specimen.

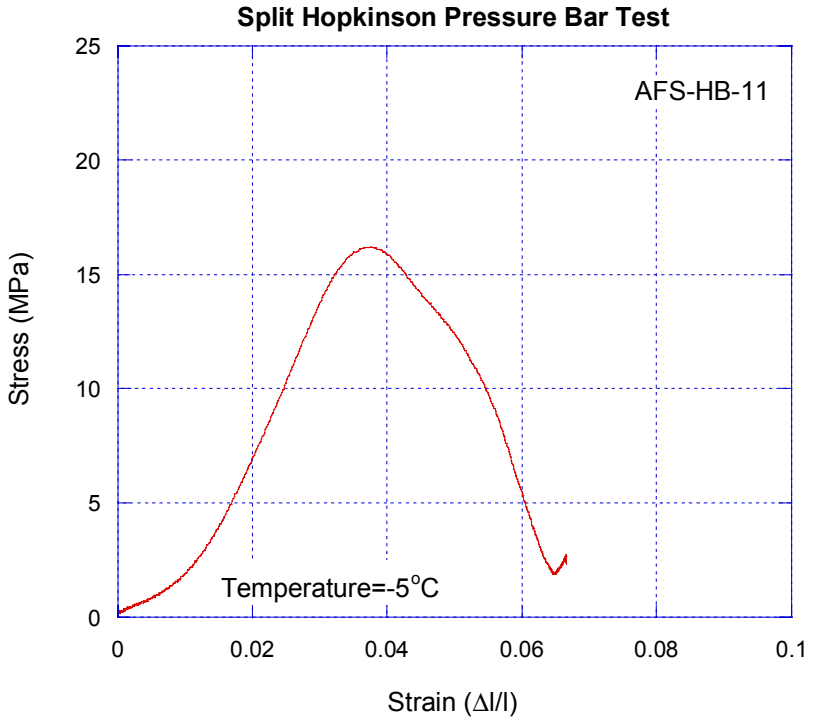

Figure 33. Typical stress-strain plot obtained from SHPB testing of an Alaskan frozen soil specimen.

Results of the SHPB testing

As summarized in Table 8, a set of 81 dynamic compression tests were conducted using a modified SHPB set-up at three temperatures (-5, -10 and –25°C). A pulse shaper made out of a felt metal disk (1 cm in diameter and 0.2 cm in thickness) was used to achieve stress equilibrium and homogeneous deformation in the specimen. In addition, we reduced the thickness to the diameter ratio of the specimen to around 0.5.

Figure 31 shows a typical raw record from the SHPB testing of a frozen soil specimen. Shown are the incident wave, ε_i, reflected wave, ε_r, from the interface a (Figure 28) and the transmitted wave, ε_t, through interface b (Figure 28). Based on the SHPB equations, histories of strain and strain rate of the specimen under dynamic loading were calculated and shown in Figure 32. Using the pulse shaping method, we were able to obtain the non-dispersive wave with the peak strain rate matching the peak stress, in most tests. Finally, by plotting $\varepsilon = \frac{2C_0}{L}\int_0^t \varepsilon_r dt$ against $\sigma_b = E\frac{A}{A_s}(\varepsilon_t)$ or $\sigma_a = E\frac{A}{A_s}(\varepsilon_i + \varepsilon_r)$, a complete stress-strain curve of the specimen under dynamic loading (Figure 33) could be constructed. The strain rate ranges from up to 1.35×10^3 /s and averages around 5.5×10^2 /s. The peak stress was attained from 0.5 to 4 % strain. From the stress-strain plot, the peak stress and the Young's modulus can be obtained at dynamic strain rates.

As shown in Figure 34, the strength of Alaskan frozen soil is weakly dependent on density for different temperatures. This dependency has been reported in other geomaterials under dynamic strain rate conditions (Olsson, 1991). However, the Young's modulus was nearly independent of density (see Figure 35).

The strength of Alaskan frozen soil was plotted against the strain rate ranging from 10^{-4}/s and 10^3/s at two different temperatures (-5 and –25°C). Figure 36 shows the strength data obtained from three types of tests: the uniaxial compression tests (Table 5) with strain rate around 10^{-4}/s, the quasi-dynamic compression tests (Table 7) with strain rate around 10/s and the SHPB testing (Table 8) with strain rate around 10^3/s. A great deal of scatter was exhibited in the strength at a given strain rate. The scatter was probably due to the results of consolidating all strength data derived from specimens with different densities. In Figure 36, general trend of strength increasing with the strain-rate is observed. Notice that the strength is a function of temperature, as indicated from Figures 27 and 36. As suggested in Figure 36, it appears there exists a trade-off between the strain rate and temperature in estimating the strength of the frozen soil. This result may have an impact on the laboratory investigation of frozen soil under dynamic strain conditions. The material constants, describing the deformation and failure of frozen soil under the dynamic strain rate (>10^3/s) condition at higher temperature (>-5°C), may be obtained from an experimental database comprising data from tests conducted under the quasi-static strain rate at a relatively lower temperature.

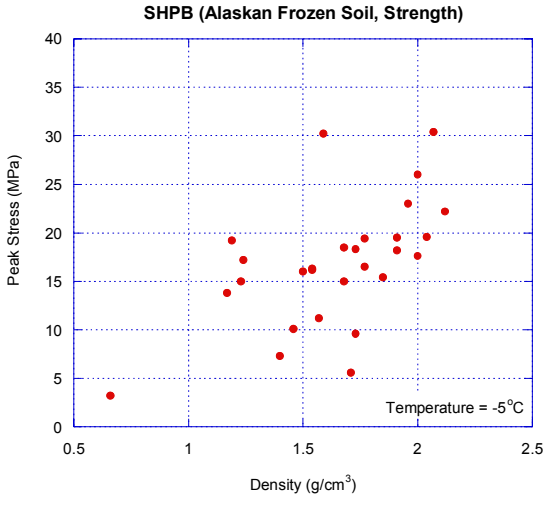

(a)

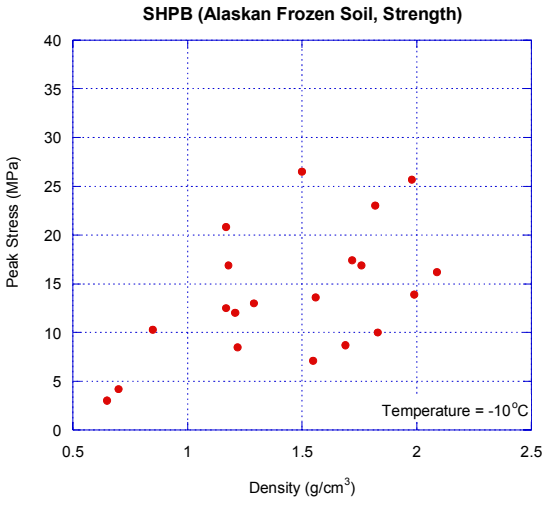

(b)

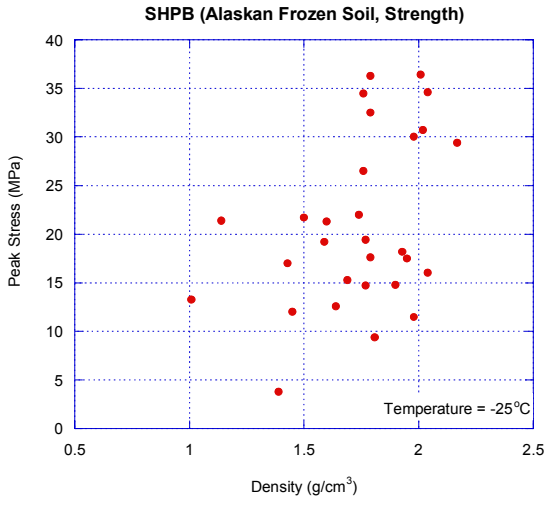

(c)

Figure 34. Variations of the strength of the Alaskan frozen soil with respect to density at different temperatures: (a) at -5°C (b) at -10°C and (c) at -25°C.

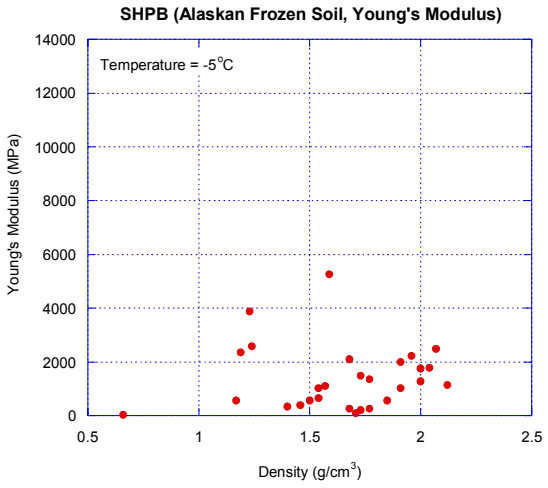

(a)

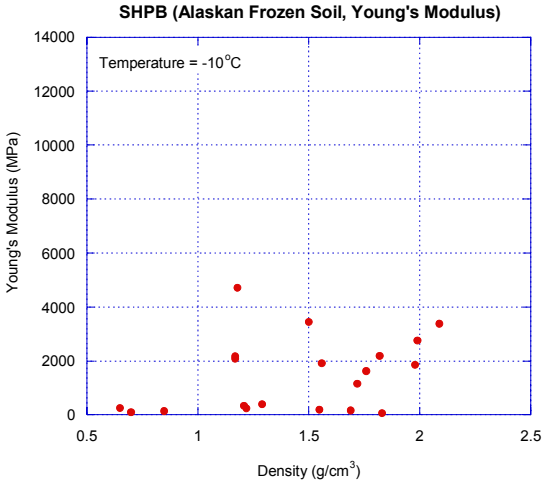

(b)

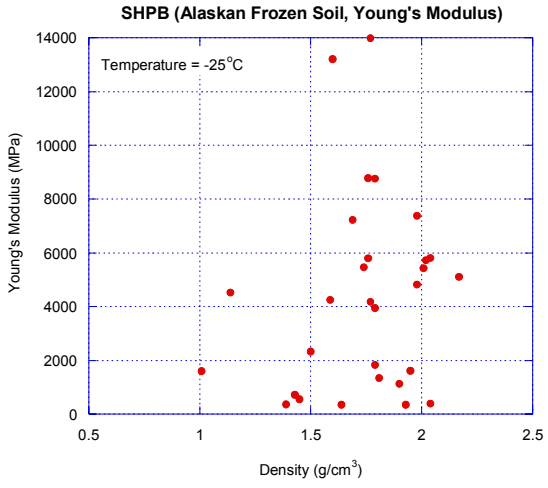

(c)

Figure 35. Variations of the Young's Modulus of the Alaskan frozen soil with respect to density at different temperatures: (a) at -5°C (b) at -10°C and (c) at -25°C.

Table 8. Summary of split Hopkinson pressure bar tests of Alaskan frozen soil.

Test No.	Core ID	Diameter (cm)	Length (cm)	Weight (g)	T (^{o}C)	Conversion Factor-input (mstrain /v)	Conversion Factor-output (mstrain /v)	Strain Rate (s^{-1})	Mean Strain Rate (s^{-1})	Density (g/cm^3)	Peak Stress (MPa)	E (MPa)
AFS-HB-01	AFS-12-B1	2.29	1.32	3.50	-10	2332	2241	510	255	0.85	10.3	140
AFS-HB-02	AFS-14-F1	2.21	1.30	6.56	-5	2332	2241	280	140	1.71	5.6	90
AFS-HB-03	AFS-14-F2	2.24	1.17	6.60	-5	2332	2241	600	300	1.68	15	270
AFS-HB-04	AFS-12-B2	2.26	1.02	2.65	-5	2332	2241	610	305	0.66	3.2	30
AFS-HB-05	AFS-14-F3	2.26	0.97	4.70	-10	2349	2276	770	385	1.17	12.5	2080
AFS-HB-06	AFS-12-B3	2.21	1.02	2.50	-10	2349	2276	830	415	0.65	3	250
AFS-HB-07	AFS-14-F4	2.24	0.94	5.05	-10	2349	2276	1350	675	1.29	13	400
AFS-HB-08	AFS-12-B4	2.21	1.12	2.70	-10	2349	2276	500	250	0.70	4.2	100
AFS-HB-09	AFS-10-A5	2.13	1.22	4.26	-5	2242	2235	500	250	1.19	19.2	2350
AFS-HB-10	AFS-10-A6	2.11	1.24	4.09	-5	2242	2235	770	385	1.17	13.8	570
AFS-HB-11	AFS-11-C7	2.03	1.17	5.01	-5	2242	2235	810	405	1.54	16.2	650
AFS-HB-12	AFS-11-C8	2.11	1.14	5.49	-5	2242	2235	660	330	1.57	11.2	1110
AFS-HB-13	AFS-09-BC1	2.24	1.19	6.80	-5	2236	2256	230	115	1.73	9.6	210
AFS-HB-14	AFS-09-BC2	2.24	1.19	7.29	-5	2236	2256	NA	NA	1.86	NA	NA
AFS-HB-15	AFS-14-B1	2.24	1.19	6.06	-5	2236	2256	530	265	1.54	16.3	1020
AFS-HB-16	AFS-14-B2	2.21	1.14	5.37	-5	2236	2256	280	140	1.40	7.3	330
AFS-HB-17	AFS-11-C6	2.06	1.17	5.71	-10	2273	2272	910	455	1.72	17.4	1160
AFS-HB-18	AFS-11-C5	2.08	1.12	5.28	-10	2273	2272	550	275	1.55	7.1	200
AFS-HB-19	AFS-10-G1	2.24	1.19	7.80	-10	2273	2272	830	415	1.99	13.9	2760
AFS-HB-20	AFS-10-G2	2.24	1.32	8.20	-10	2273	2272	390	195	2.09	16.2	3370
AFS-HB-21	AFS-10-A1	2.11	1.17	4.08	-10	2269	2252	560	280	1.17	20.8	2170
AFS-HB-22	AFS-10-A2	2.11	1.17	4.11	-10	2269	2252	500	250	1.18	16.9	4700
AFS-HB-23	AFS-14-B3	2.21	1.14	4.68	-10	2269	2252	620	310	1.22	8.5	230
AFS-HB-24	AFS-14-B4	2.21	1.14	4.64	-10	2269	2252	430	215	1.21	12	340

(Continued on the next page.)

Table 8. Summary of split Hopkinson pressure bar tests of Alaskan frozen soil (Continued).

Test	Core	Diameter	Length	Weight	T	Conversion	Conversion	Strain	Mean	Density	Peak	E

No.	ID	(cm)	(cm)	(g)	(^{o}C)	Factor-input (mstrain /v)	Factor-output (mstrain /v)	Rate (s^{-1})	Strain Rate (s^{-1})	(g/cm^3)	Stress (MPa)	(MPa)
AFS-HB-25	AFS-09-BC3	2.21	1.19	6.50	-10	2269	2252	80	40	1.69	8.7	160
AFS-HB-26	AFS-09-BC4	2.18	1.22	6.84	-10	2269	2252	NA	NA	1.83	10	70
AFS-HB-27	AFS-11-C1	2.08	1.17	5.77	-25	2289	2290	650	325	1.69	15.3	7230
AFS-HB-28	AFS-11-C2	2.06	1.19	5.45	-25	2289	2290	650	325	1.64	12.6	350
AFS-HB-29	AFS-10-G3	2.24	1.24	8.00	-25	2289	2290	610	305	2.04	16	400
AFS-HB-30	AFS-10-G4	2.21	1.24	7.58	-25	2289	2290	240	120	1.98	11.5	7370
AFS-HB-31	AFS-10-G5	2.24	1.09	7.59	-25	2289	2290	440	220	1.93	18.2	350
AFS-HB-32	AFS-10-A3	2.16	1.22	4.16	-25	2289	2267	410	205	1.14	21.4	4520
AFS-HB-33	AFS-10-A4	2.16	1.04	3.68	-25	2289	2267	780	390	1.01	13.3	1590
AFS-HB-34	AFS-11-C3	2.06	1.17	4.81	-25	2289	2267	540	270	1.45	12	550
AFS-HB-35	AFS-11-C4	2.06	1.09	4.77	-25	2289	2267	570	285	1.43	17	730
AFS-HB-36	AFS-03-A	2.21	1.19	5.59	-5	2873	2475	810	405	1.46	10.1	400
AFS-HB-37	AFS-03-A	2.21	1.30	5.74	-5	2873	2475	750	375	1.50	16	560
AFS-HB-38	AFS-09-E	2.18	1.24	5.96	-5	2873	2475	360	180	1.59	30.2	5270
AFS-HB-39	AFS-10-D	2.29	1.24	7.58	-5	2873	2475	570	285	1.85	15.4	570
AFS-HB-40	AFS-04-E	2.26	1.27	7.85	-5	2873	2475	580	290	1.96	23	2220
AFS-HB-41	NA	NA	NA	NA	NA	2873	2475	NA	NA	NA	NA	NA
AFS-HB-42	AFS-15-C	2.24	1.27	7.50	-5	2873	2475	640	320	1.91	18.2	1030
AFS-HB-43	AFS-07-D	2.24	1.22	6.93	-5	2873	2475	550	275	1.77	19.4	1350
AFS-HB-44	AFS-07-D	2.24	1.12	6.59	-5	2873	2475	410	205	1.68	18.5	2100
AFS-HB-45	NA	NA	NA	NA	NA	2873	2475	NA	NA	NA	NA	NA
AFS-HB-46	NA	NA	NA	NA	NA	2873	2475	NA	NA	NA	NA	NA
AFS-HB-47	AFS-12-D	2.21	1.27	7.83	-5	2873	2475	470	235	2.04	19.6	1790
AFS-HB-48	AFS-12-D	2.18	1.30	7.48	-5	2873	2475	700	350	2.00	17.6	1280

(Continued on the next page.)

Table 8. Summary of split Hopkinson pressure bar tests of Alaskan frozen soil (Continued).

Test No.	Core ID	Diameter (cm)	Length (cm)	Weight (g)	T (^{o}C)	Conversion Factor-input (mstrain /v)	Conversion Factor-output (mstrain /v)	Strain Rate (s^{-1})	Mean Strain Rate (s^{-1})	Density (g/cm^3)	Peak Stress (MPa)	E (MPa)

AFS-HB-49	AFS-04-A	2.29	1.24	5.07	-5	2873	2475	460	230	1.24	17.2	2580
AFS-HB-50	AFS-04-A	2.18	1.22	4.61	-5	2873	2475	270	135	1.23	15	3870
AFS-HB-51	AFS-10-C	2.16	1.24	6.98	-5	2873	2475	560	280	1.91	19.5	2000
AFS-HB-52	AFS-09-E	2.31	1.24	7.25	-5	2873	2475	580	290	1.73	18.3	1480
AFS-HB-53	AFS-02-E	2.18	1.30	7.96	-5	2873	2475	550	275	2.12	22.2	1140
AFS-HB-54	AFS-02-E	2.18	1.27	7.49	-5	2873	2475	650	325	2.00	26	1750
AFS-HB-55	AFS-04-E	2.29	1.30	8.49	-5	2873	2475	370	185	2.07	30.4	2490
AFS-HB-56	AFS-13-E	2.18	1.27	6.65	-5	2873	2475	620	310	1.77	16.5	270
AFS-HB-57	AFS-03-A	2.26	1.32	5.56	-25	2851	2488	430	215	1.39	3.8	370
AFS-HB-58	AFS-03-A	2.18	1.24	5.94	-25	2851	2488	360	180	1.59	19.2	4250
AFS-HB-59	AFS-03-A	2.29	1.27	6.14	-25	2851	2488	580	290	1.50	21.7	2330
AFS-HB-60	AFS-09-E	2.34	1.22	6.88	-25	2851	2488	180	90	1.60	21.3	13200
AFS-HB-61	AFS-09-E	2.34	1.32	7.78	-25	2851	2488	450	225	1.81	9.4	1340
AFS-HB-62	AFS-10-D	2.29	1.22	7.24	-25	2851	2488	390	195	1.76	34.5	5790
AFS-HB-63	AFS-10-D	2.29	1.30	7.33	-25	2851	2488	450	225	1.79	36.3	8760
AFS-HB-64	AFS-12-D	2.26	1.32	8.10	-25	2851	2488	340	170	2.02	30.7	5720
AFS-HB-65	AFS-12-D	2.24	1.24	7.90	-25	2851	2488	400	200	2.01	36.4	5420
AFS-HB-66	AFS-15-C	2.21	1.32	8.33	-25	2851	2488	380	190	2.17	29.4	5100
AFS-HB-67	AFS-15-C	2.24	1.32	7.99	-25	2851	2488	310	155	2.04	34.6	5810
AFS-HB-68	AFS-04-E	2.26	1.27	7.11	-25	2851	2488	170	85	1.77	19.4	13970
AFS-HB-69	AFS-07-D	2.21	1.30	6.78	-25	2851	2488	260	130	1.77	14.7	4170
AFS-HB-70	AFS-07-D	2.21	1.30	6.88	-25	2851	2488	440	220	1.79	17.6	1830
AFS-HB-71	AFS-02-E	2.24	1.27	7.03	-25	2851	2488	240	120	1.79	32.5	3950
AFS-HB-72	AFS-02-E	2.21	1.27	7.46	-25	2851	2488	770	385	1.95	17.5	1610

(Continued on the next page.)

Table 8. Summary of split Hopkinson pressure bar tests of Alaskan frozen soil (Continued).

Test No.	Core ID	Diameter (cm)	Length (cm)	Weight (g)	T (^{o}C)	Conversion Factor-input (mstrain /v)	Conversion Factor-output (mstrain /v)	Strain Rate (s^{-1})	Mean Strain Rate (s^{-1})	Density (g/cm^3)	Peak Stress (MPa)	E (MPa)
AFS-HB-73	AFS-04-A	2.18	1.32	6.58	-25	2851	2488	570	285	1.76	26.5	8770
AFS-HB-74	AFS-04-A	2.18	1.32	6.53	-25	2851	2488	730	365	1.74	22	5460
AFS-HB-75	AFS-13-E	2.16	1.30	6.96	-25	2851	2488	850	425	1.90	14.8	1120

AFS-HB-76	AFS-10-C	2.18	1.27	7.43	-25	2851	2488	800	400	1.98	30	4820
AFS-HB-77	AFS-03-A	2.18	1.24	5.85	-10	2873	2475	850	425	1.56	13.6	1910
AFS-HB-78	AFS-03-A	2.21	1.27	5.75	-10	2873	2475	720	360	1.50	26.5	3440
AFS-HB-79	AFS-12-D	2.26	1.27	7.93	-10	2873	2475	800	400	1.98	25.7	1860
AFS-HB-80	AFS-02-E	2.24	1.19	7.16	-10	2873	2475	640	320	1.82	23	2190
AFS-HB-81	AFS-07-D	2.18	1.17	6.60	-10	2873	2475	470	235	1.76	16.9	1630

SHPB input and output bar material - Aluminum 7075-T6 extrusion

Al. Bar wave velocity = 6.3 km / s

Al. Bar Young's modulus = 72 GPa

Al. Bar diameter = 2.54 cm

E=Young's Modulus; T=Temperature

Mean strain rate=0.5*strain rate

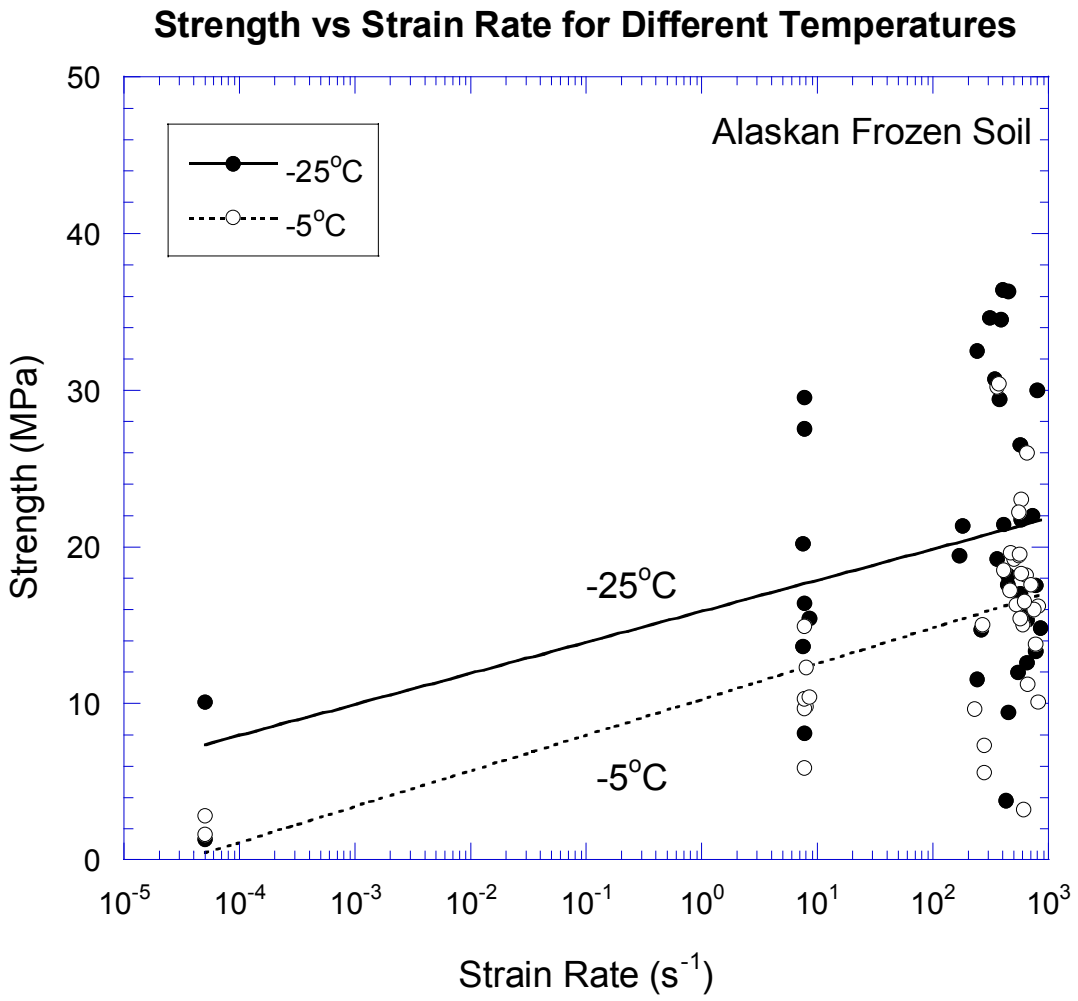

Figure 36. Strength of the Alaskan frozen soil plotted against strain rate at two different temperatures. Trade-offs between the temperature and strain rate were observed for the strength of the Alaskan frozen soil.

5. Constitutive Modeling

Laboratory material testing showed that Alaskan frozen soil exhibits pressure and temperature dependence, rate sensitivity, anisotropy, brittle and ductile behavior, volumetric compaction, and dilation. A constitutive equation capable of modeling such a complex material is the rate-sensitive, anisotropic version of a plasticity model being developed by Fossum and Fredrich (2000). This model includes high strain-rate sensitivity and anisotropy in both the elastic and plastic regimes. The model is defined through a continuous yield and loading surface for unified dilation and compaction phenomena. Included are a pore collapse mechanism, shear failure mechanism, and a cleavage failure mechanism.

For frozen soil, it is sufficient to limit the anisotropy to transverse isotropy. In the following, it is assumed that anisotropy occurs in the 11 direction as depicted in Figure 37.

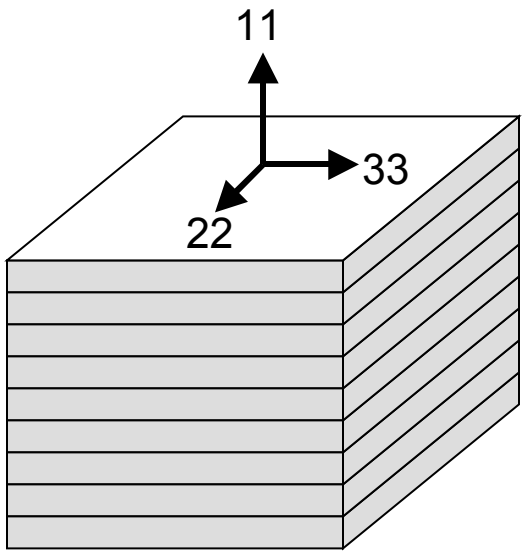

Figure 37. The constitutive model is developed for a transversely isotropic material

In general, the tensor form of Hooke's law is written in terms of a fourth-order coefficient matrix, C_{ijkl}, as

$$\boldsymbol{\sigma}_{ij} = C_{ijkl}\boldsymbol{\varepsilon}_{kl}$$

If the stresses $\boldsymbol{\sigma}_{ij}$ and elastic strains $\boldsymbol{\varepsilon}^{e}_{kl}$ are ordered according to ($\boldsymbol{\sigma}_{i}$, $\boldsymbol{\varepsilon}^{e}_{i}$, *i = 11, 22, 33, 12, 13, 23*), then Hooke's Law can be written in terms of a second-order coefficient matrix, which for transversely isotropic materials is given by

$$\begin{Bmatrix} \sigma_{11} \\ \sigma_{22} \\ \sigma_{33} \\ \sigma_{12} \\ \sigma_{13} \\ \sigma_{23} \end{Bmatrix} = \begin{bmatrix} C_{11} & C_{12} & C_{12} & 0 & 0 & 0 \\ C_{12} & C_{33} & C_{23} & 0 & 0 & 0 \\ C_{12} & C_{23} & C_{33} & 0 & 0 & 0 \\ 0 & 0 & 0 & C_{44} & 0 & 0 \\ 0 & 0 & 0 & 0 & C_{44} & 0 \\ 0 & 0 & 0 & 0 & 0 & C_{33} - C_{23} \end{bmatrix} \begin{Bmatrix} \varepsilon_{11}^{e} \\ \varepsilon_{22}^{e} \\ \varepsilon_{33}^{e} \\ \varepsilon_{12}^{e} \\ \varepsilon_{13}^{e} \\ \varepsilon_{23}^{e} \end{Bmatrix}$$

The rate form of the frozen soil plasticity model is then written as

$$\dot{\boldsymbol{\varepsilon}}_i^{vp} = \frac{1}{\eta} C_{ij}^{-1} \left(\boldsymbol{\sigma}_j - \overline{\boldsymbol{\sigma}}_j \right)$$

where an overbar denotes the inviscid solution and η is a material parameter called relaxation time. The state variables, *q*, are governed by evolution equations of the form

$$\dot{q} = \frac{-1}{\eta} \left(q - \overline{q} \right)$$

The inviscid solution is determined from the rate-independent plasticity formulation. In this formulation, a single anisotropic flow rule governs compaction and dilation,

$$\dot{\boldsymbol{\varepsilon}}_i^{p} = \dot{\boldsymbol{\gamma}} \frac{\partial f}{\partial \overline{\boldsymbol{\sigma}}_i}$$

written in terms of a continuous yield and loading surface, *f,* for unified dilation and compaction phenomena and a consistency parameter $\dot{\boldsymbol{\gamma}}$. The yield function is given by

$$f\left(\boldsymbol{\Xi}, \boldsymbol{\Psi} \right) = \boldsymbol{\Psi} - \left(F_s \right)^2 F_c = 0$$

in which F_c represents the pore collapse mechanism,

$$F_c\left(\boldsymbol{\Xi}, \boldsymbol{\kappa} \right) = 1 + \frac{\left(\boldsymbol{\Xi} - L \right) \left\{ \left| \boldsymbol{\Xi} - L \right| - \left(\boldsymbol{\Xi} - L \right) \right\}}{2\left(X - L \right)^2}$$

and L is a hardening state variable; F_s represents the brittle shear failure mechanism,

$$F_s = \sqrt{\boldsymbol{\Psi}} \Big|_f = A + C \exp(B \boldsymbol{\Xi})$$

and

Ξ and Ψ are anisotropic stress potentials given by

$$\Xi = \bar{\sigma}_{11} + a(\bar{\sigma}_{22} + \bar{\sigma}_{33})$$

and

$$\Psi = \frac{b}{6}\left[(\bar{\sigma}_{11} - \bar{\sigma}_{22})^2 + (\bar{\sigma}_{11} - \bar{\sigma}_{33})^2\right] + \frac{1}{6}(\bar{\sigma}_{22} - \bar{\sigma}_{33})^2 + \frac{c}{2}\left[(\bar{\sigma}_{12}^2 + \bar{\sigma}_{21}^2) + (\bar{\sigma}_{13}^2 + \bar{\sigma}_{31}^2)\right] + \frac{(b+2)}{6}(\bar{\sigma}_{23}^2 + \bar{\sigma}_{32}^2)$$

in which *a*, *b*, and *c* are material parameters.

The consistency parameter, $\dot{\gamma}$, is given by

$$\dot{\gamma} = \frac{\left\{\frac{9K}{(1+2a)}\frac{\partial f}{\partial \Xi} - cC_{44}\frac{(1-a)}{(1+2a)}\xi_{11}\frac{\partial f}{\partial \Psi}\right\}\dot{\varepsilon}_{kk} + cC_{44}\frac{\partial f}{\partial \Psi}\xi_{ij}\dot{\varepsilon}'_{ij}}{\left[(1+2a)^2 C_{23} + \frac{3cC_{44}\{2ab(1+a)-1\}}{b(2+b)}\right]\left(\frac{\partial f}{\partial \Xi}\right)^2 + cC_{44}\left(\frac{\partial f}{\partial \Psi}\right)^2 \xi_{ij}\xi_{ij} - (1+2a)\frac{\partial f}{\partial \Xi}\frac{\partial f}{\partial \varepsilon^p_{kk}}}$$

where $\dot{\varepsilon}'_{ij}$ denotes deviatoric strain, and ξ_{ij} are the inviscid stress derivatives of Ψ. The consistency parameter follows from the consistency condition of Prager,

$$\dot{f} = \frac{\partial f}{\partial \bar{\sigma}_{ij}}\dot{\bar{\sigma}}_{ij} + \frac{\partial f}{\partial \bar{q}}\dot{\bar{q}} = 0$$

The frozen soil model can be reduced to an isotropic model and also to a quasi-static model. The data presented in the previous sections were used to fit the material parameters of the model.

The brittle shear-failure parameters were determined from tests AFS-TA-01, AFS-TA-02, and AFS-TA-03. The parameters *A, B,* and *C* were determined from this data. The parameters *a, b,* and *c* have the value *one* because these specimens are isotropic. The model-fit to this data is shown in Figure 38, together with the model parameters.

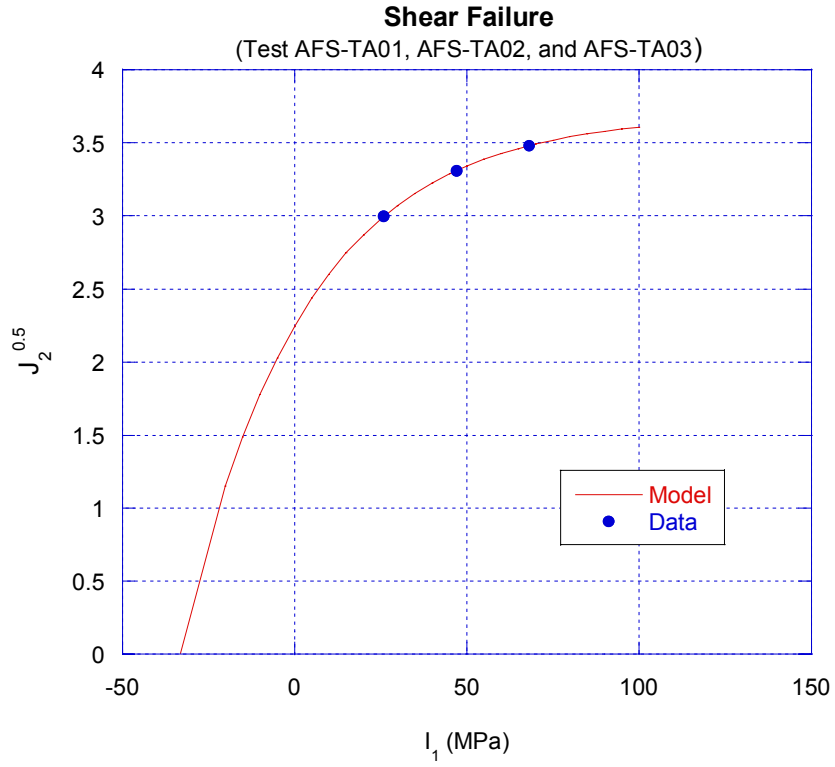

A = 3.69 MPa
B = 2.82E-02 1/MPa
C = 1.45 MPa
a = 1.0
b = 1.0
c = 1.0

Figure 38. Alaskan frozen soil model vs. measured brittle shear-failure data.

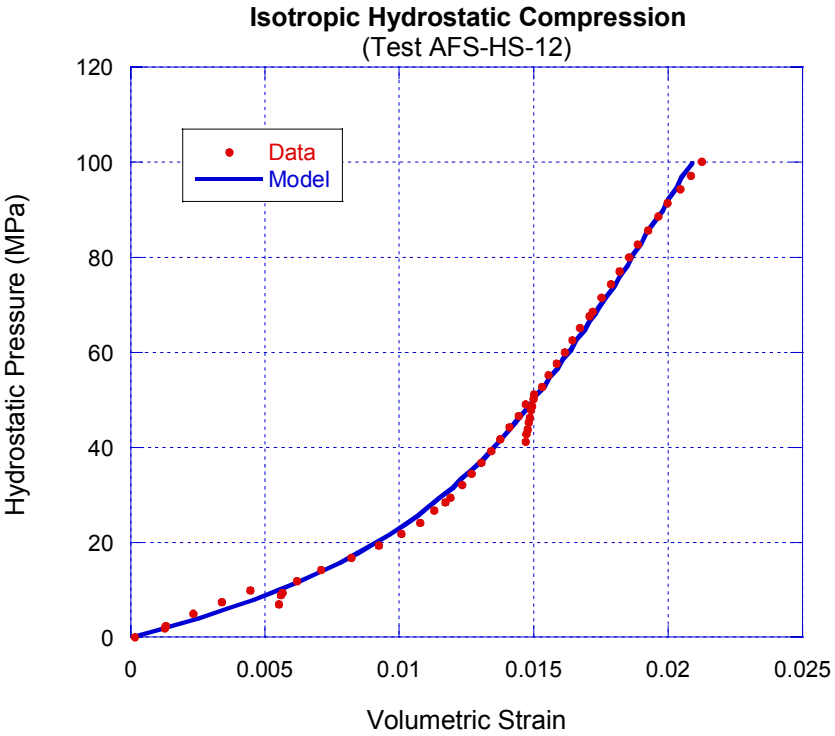

C_{11} = 9083.2 MPa
C_{33} = 9083.2 MPa
C_{44} = 99.09 MPa
C_{12} = 8984.1 MPa
C_{23} = 8984.1 MPa
D_1 = 1.93E-02 1/MPa
D_2 = 1.92E-05 1/MPa^2
W = 9.82E-03
X_0 = -0.108 MPa
a = 1.0
b = 1.0
c = 1.0
η = 0 s

Figure 39. Alaskan frozen soil model vs. measured isotropic hydrostatic compression data.

The isotropic compaction parameters were determined from an isotropic hydrostatic compression test. The data were obtained from test specimen AFS-HS-12. Figure 39 shows the model fitted to this data. Because this test was quasi-static, the relaxation time was set to a very high value.

The shape parameter, R, and the elastic parameter C_{44}, were determined from an isotropic triaxial compression test, AFS-TA-03, conducted at 20.7 MPa confining pressure. Figure 40 shows the model fitted to this data.

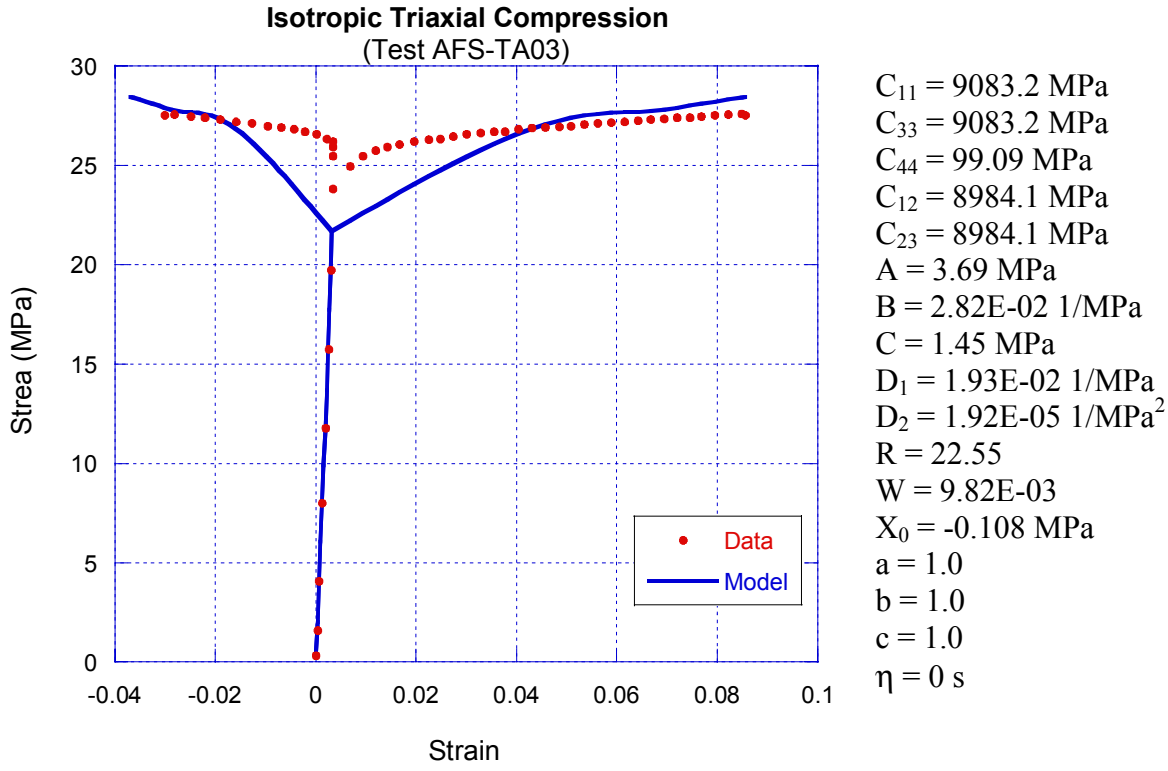

Figure 40. Alaskan frozen soil model versus measured isotropic triaxial compression data.

This completes the evaluation of all the isotropic, quasi-static material parameters. All the tests used in this evaluation were conducted at –10C. It should be noted that in the isotropic case only two of the five elastic constants are independent. These are C_{11} and C_{12}. Constant C_{44} is given by $C_{11} - C_{12}$. Moreover, the elastic bulk modulus, K, and Shear modulus, G, are given by $K = C_{12} + C_{44}/3$ and $G = C_{44}/2$, which give values of 9017.1 MPa and 49.55 MPa, respectively.

The shape of the yield surface is shown in Figure 41. The load path shown corresponds to the triaxial compression test of Figure 40.

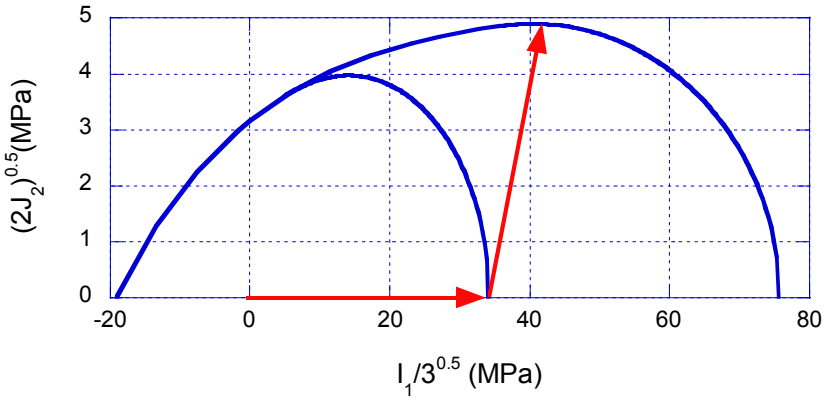

Figure 41. Yield surface and load path followed during a triaxial compression test.

The relaxation time was determined from a split Hopkinson bar test that produced a very high strain rate. The data point was obtained from test AFS-HB-05. For comparison, the model was used to predict a quasi-static, unconfined compression test. None of the unconfined compression tests were taken to failure in the laboratory. Figure 42 shows these results based on strain rate approximated from the laboratory data (Figure 43).

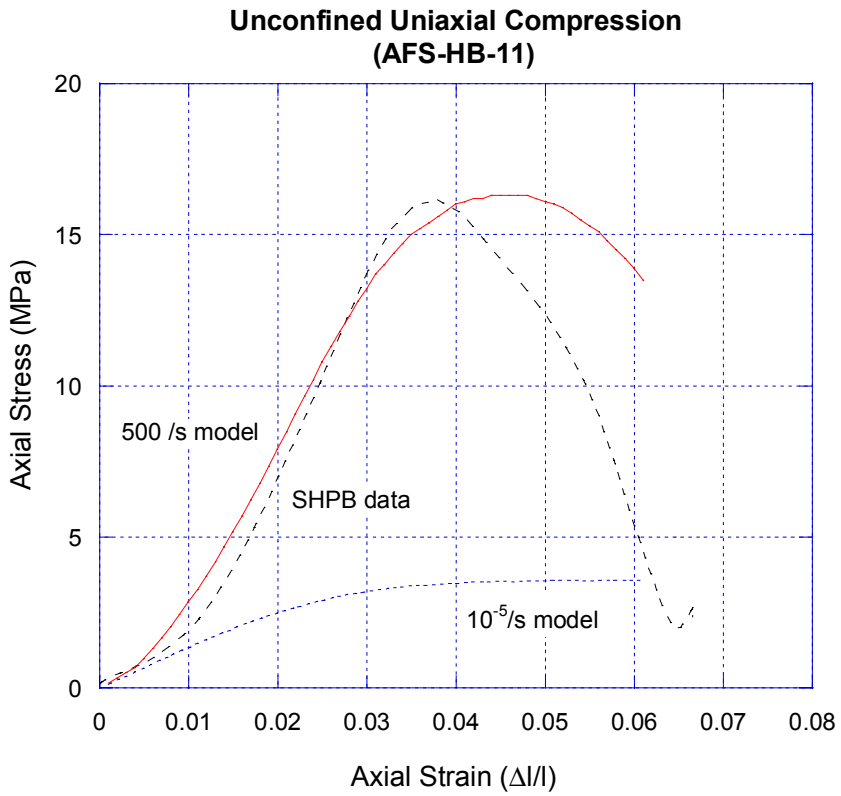

C_{11} = 9083.2 MPa
C_{33} = 9083.2 MPa
C_{44} = 99.09 MPa
C_{12} = 8984.1 MPa
C_{23} = 8984.1 MPa
A = 3.69 MPa
B = 2.82E-02 1/MPa
C = 1.45 MPa
D_1 = 1.93E-02 1/MPa
D_2 = 1.92E-05 1/MPa^2
R = 22.55
W = 9.82E-03
X_0 = -0.108 MPa
a = 1.0
b = 1.0
c = 1.0
η = 6.8E-7 s

Figure 42. Comparison of a high-rate model calculation with a quasi-static model calculation and a split Hopkinson bar experimental result.

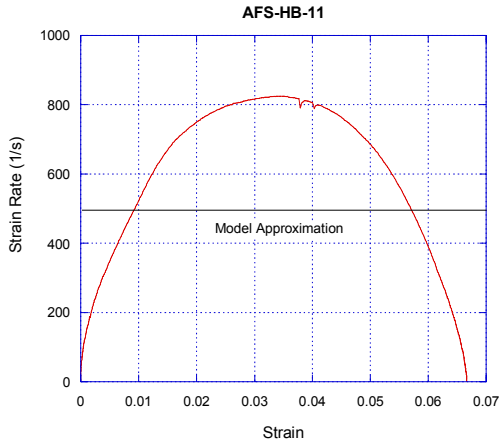

Figure 43. Approximated strain rate used for model calculation.

Some of the experimental data obtained from the Alaskan frozen soil showed anisotropy. An anisotropic hydrostatic compression test was used to estimate the anisotropic parameters C_{11}, C_{33}, C_{44}, C_{12}, C_{23}, a, b, and c. The data were taken from test AFS-HS-07. Figure 44 shows the model fitted to these results.

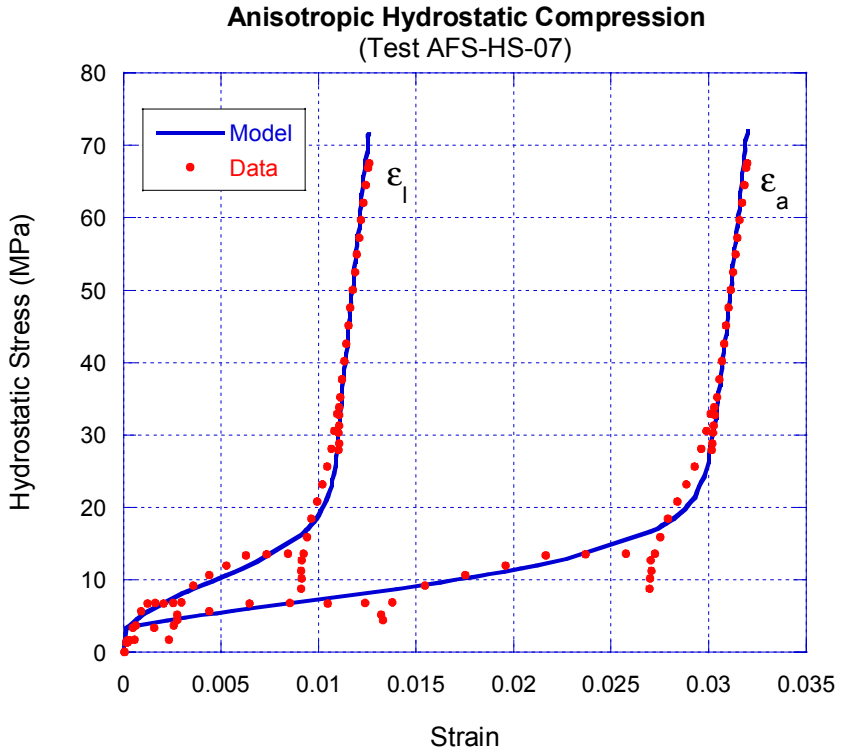

C_{11} = 8705.8 MPa
C_{33} = 8711.8 MPa
C_{44} = 99.09 MPa
C_{12} = 8698.2 MPa
C_{23} = 8692.1 MPa
A = 3.69 MPa
B = 2.82E-02 1/MPa
C = 1.45 MPa
D_1 = 1.72E-02 1/MPa
D_2 = 9.37E-04 1/MPa^2
R = 22.55
W = 4.88E-02
X_0 = -10.42 MPa
a = 1.027
b = 13.1
c = 1.0
η = 0 s

Figure 44. Alaskan frozen soil model versus measured quasi-static anisotropic hydrostatic compression data.

The model is quite capable of reproducing a wide range of observed experimental behavior of Alaskan frozen soil. Future enhancements of the model may include the capability to model temperature dependence and phase transformations.

6. Conclusions

To obtain a well-determined data set of Alaskan frozen soil, a series of quasi-static, quasi-dynamic and dynamic compression tests was conducted using unique high-pressure, low-temperature apparatus and the split Hopkinson pressure bar (SHPB). The results from laboratory constitutive experiments can be summarized as follows:

- Alaskan Frozen Soil is a temperature dependent, anisotropic material. The density of the frozen soil depends on the depth of the soil measured from the surface. The near-surface layer (< 1 m) consists of a low density organic material, layered subparallel to the surface.

- The material properties of Alaskan Frozen Soil are largely dependent on the density of the soil.

- The material properties database for Alaskan Frozen Soil has been established based on five types of laboratory tests: Brazilian indirect tension test, hydrostatic compression test, uniaxial compression test conducted at the strain rate of around 10^{-4}/s, quasi-dynamic compression test conducted at the strain rate of around 10/s, and the SHPB test conducted at the strain rate of around 10^{3}/s. The results are summarized in Tables 3 through 8.

- The ice trapped in the Alaskan Frozen Soil may have been transformed into water near 100 MPa confining pressure at -10ºC. The phase transformation may affect the material properties of Alaskan Frozen Soil under the high impact pressure.

- Alaskan frozen soil compacts and then dilates during triaxial testing.

- A trade-off between the strain rate and the temperature exists in estimating the strength of the frozen soil.

References

ASTM D3967, Standard Test Method for Splitting Tensile Strength of Intact Rock Core Specimens, American Society for Testing and Materials, 1995.

ASTM D4543, Standard Practice for Preparing Rock Core Specimens and Determining Dimensional and Shape Tolerances, American Society for Testing and Materials, 1995.

Chamberlain, E., Groves, C. and R. Perham, Mechanical Behaviour of Frozen Earth Materials under High Pressure Triaxial Test Condition, Geotechique, 22, No. 3, 469-481, 1972.

Durham, W.B., Heard, H.C. and S.H. Kirby, Experimental Deformation of Polycrystalline H_2O Ice at High Pressure and Low Temperature: Preliminary Results, JGR, Vol.88, 377-392, 1983.

Fossum, A.F. and J.T. Fredrich, Cap Plasticity Models and Compactive and Pliant Pre-Failure Deformation, Proceedings of the Fourth North American Rock Mechanics Symposium, NARMS 2000, Seattle, Washington, 1169-1176, 2000.

Frew D.J., Forrestal, M.J. and W. Chen, Pulse Shaping Techniques for Testing Brittle Materials with a Split Hopkinson Pressure Bar, Experimental Mechanics, 2002.

Gratz, E. T. and E. M. Schulson, The Deformation of Cubes of Frozen Soil Loaded under Triaxial Compression, Final Report, Project No. AN-2014, 94 p., Thayer School of Engineering, Dartmouth College, Hanover, New Hampshire, 1996.

Hardy, R., Event Triggered Data Acquisition in the Rock Mechanics Laboratory, Sandia Report SAND93-0256, UC-403, Sandia National Laboratories, Albuquerque NM., 1993.

Jaeger, J.C. and N.G.W. Cook, Fundamentals of Rock Mechanics, 102-106, Methuen, London, England, 1969.

Kolsky, H., An Investigation of the Mechanical Properties of Materials at Very High Rates of Strain, Proc. Roy. Phys. Soc., B62, 676-700, 1949.

Lindholm, U.S., Some Experiments with the Split Hopkinson Pressure Bar, J. Mech. Phys. Solids, Vol.12, 317-335, Pergamon, 1964.

Olsson, W.A., The Compressive Strength of Tuff as a Function of Strain Rate from 10^{-6} to 10^{3}/sec, Int. J. Rock Mech. Min. Sci. & Geomech. Abstr. Vol. 28, No.1, 115-118, 1991.

Ueda, H., Sellmann, P. and G. Abele, USA CRREL Snow and Ice Testing Equipment, US Army Corps of Engineers, CREEL special report 146, 1975.

Zeuch, D. H., Lee, M.Y., Costin L. S., Wawersik, W. R., Grazier J. M., Bronowski D. R., and R. D. Hardy, A High-Pressure, Low-Temperature Triaxial Test Apparatus, In International Mechanical Engineering Congress and Exposition of the ASME, Nashville, Tennessee, 1999.

APPENDIX

Supplemental CD for archived test records and data.

Table A-1. List of Windows Meta Files (*.wmf) archived in the supplemental CD.

Folder Name	File Name	File Type	No. of Files
/AFS-Figures/Hydrostatic Compression	AFS-HS-01.wmf to AFS-HS-17.wmf	Test records from hydrostatic compression tests	17
/AFS-Figures/Brazilian Tension	AFS-BR-01.wmf to AFS-HS-17.wmf	Test records from Brazilian tension tests	17
/AFS-Figures/Uniaxial Compression	AFS-UC-01.wmf to AFS-UC-09.wmf	Test records from uniaxial compression tests	9
/AFS-Figures/Triaxial Compression	AFS-TA-01-a.wmf to AFS-TA-01-b.wmf AFS-TA-02.wmf to AFS-TA-05.wmf AFS-TA-06-a.wmf to AFS-TA-06-e.wmf AFS-TA-07-a.wmf to AFS-TA-07-f.wmf AFS-TA-08.wmf AFS-TA-09-a.wmf to AFS-TA-09-d.wmf AFS-TA-10.wmf AFS-TA-11-a.wmf to AFS-TA-11-c.wmf AFS-TA-12.wmf AFS-TA-13-a.wmf to AFS-TA-13-d.wmf AFS-TA-14-a.wmf to AFS-TA-14-e.wmf AFS-TA-15-a.wmf to AFS-TA-15-d.wmf AFS-TA-16-a.wmf to AFS-TA-16-e.wmf	Test records from triaxial compression tests	45
/AFS-Figures/Quasi-dynamic Compression	AFS-QD-1 to 4.wmf AFS-QD-5 to 11.wmf AFS-QD-12 to 18.wmf	Test records from quasi-dynamic compression tests	3
/AFS-Figures/SHPB	AFS-HB-01-rec.wmf to AFS-HB-81-rec.wmf AFS-HB-01-sr.wmf to AFS-HB-81-sr.wmf AFS-HB-01-ss.wmf to AFS-HB-81-ss.wmf (excluding test 14, 41, 45, and 46)	*rec.wmf: test records from split Hopkinson pressure bar tests *sr.wmf: strain rate vs. time and stress vs. time plots. *ss.wmf: stress-strain plots.	231

Table A-2. List of KaleidaGraph (http://www.synergy.com) Files (*.qpc) archived in the supplemental CD.

Folder Name	File Name	File Type	No. of Files
/AFS-Data/Hydrostatic Compression	AFS-HS-01.qpc to AFS-HS-17.qpc	Test records from hydrostatic compression tests	17
/AFS-Data/Brazilian Tension	AFS-BR-01.qpc to AFS-HS-17.qpc	Test records from Brazilian tension tests	17
/AFS-Data/Uniaxial Compression	AFS-UC-01.qpc to AFS-UC-09.qpc	Test records from uniaxial compression tests	9
/AFS-Data/Triaxial Compression	AFS-TA-01-a.qpc to AFS-TA-01-b.qpc AFS-TA-02.qpc to AFS-TA-05.qpc AFS-TA-06-a.qpc to AFS-TA-06-e.qpc AFS-TA-07-a.qpc to AFS-TA-07-f.qpc AFS-TA-08.qpc AFS-TA-09-a.qpc to AFS-TA-09-d.qpc AFS-TA-10.qpc AFS-TA-11-a.qpc to AFS-TA-11-c.qpc AFS-TA-12.qpc AFS-TA-13-a.qpc to AFS-TA-13-d.qpc AFS-TA-14-a.qpc to AFS-TA-14-e.qpc AFS-TA-15-a.qpc to AFS-TA-15-d.qpc AFS-TA-16-a.qpc to AFS-TA-16-e.qpc	Test records from triaxial compression tests	45
/AFS-Data/Quasi-dynamic Compression	AFS-QD-1 to 4.qpc AFS-QD-5 to 11.qpc AFS-QD-12 to 18.qpc	Test records from quasi-dynamic compression tests	3
/AFS-Data/SHPB	AFS-HB-01-rec.qpc to AFS-HB-81-rec.qpc AFS-HB-01-sr.qpc to AFS-HB-81-sr.qpc AFS-HB-01-ss.qpc to AFS-HB-81-ss.qpc (excluding test 14, 41, 45, and 46)	*rec.qpc: test records from Split Hopkinson pressure bar tests *sr.qpc: strain rate vs. time and stress vs. time plots. *ss.qpc: stress-strain plots.	231

DISTRIBUTION

Sandia National Laboratories
P.O. Box 5800
Albuquerque, NM 87185

MS 0841	Thomas C. Bickel (9100)
MS 0751	David Bronowski (6117)
MS 0751	Laurence S. Costin (6117) (2 copies)
MS 0701	P. J. Davies, 6100
MS 0447	Kevin Eklund (2111)
MS 1174	Michael Forrestal (15414)
MS 0751	Arlo Fossum (6117) (3 copies)
MS 1174	Danny Frew (1174)
MS 9404	John Garcia (8725)
MS 0834	Justine E. Johannes (9114)
MS 0847	Joseph Jung (9126)
MS 0751	Moo Y. Lee (6117) (5 copies)
MS 0828	Martin Pilch (9133)
MS 0835	Mike McGlaun (9140)
MS 0847	Harold S. Morgan (9120)
MS 0824	Jaime L. Moya (9130) (3 copies)
MS 0482	Robert Paulsen (2109)
MS 0130	Joseph Polito (1200)
MS 0824	Arthur C. Ratzel (9110)
MS 0429	Steven J. Rottler (2100)
MS 9003	Michael O. Vahle (9900)
MS 0139	Peter J. Wilson (9902)
MS0482	Joel Wirth (2131)
MS0321	Paul Yarrington (9230)
MS 9018	Central Tech. Files, 8945-1
MS 0899	Technical Library, 9616 (2 copies)
MS 0731	823/Library, 6850 (2 copies)
MS 0612	Review and Approval Desk (9612)

P.O. Box 808
Livermore, CA 94551

Roger Logan, L-25

Los Alamos National Laboratory
P.O. Box 1663
Los Alamos, NM 87545

Bill Bearden MS F602
Steve Girrens, ESA-EA, P946
Dick Macek MS P946

Kevin C. Greenaugh
Department of Energy/Defense Programs
Director, Division of System Simulation & Validation
1000Independence Ave., SW
Washington DC 20585

Bill-Roy Harrison
Department of Energy/Defense Programs
Program Manager, Weapons Systems Engineering Certification Campaign
19901 Germantown Rd
Germantown, MD 20874

Diane Bird
Weapons Assessments and Development
Supervisory General Engineer
1000 Independence Ave.
NA-115.1
Washington DC 20585